https://doi.org/10.5194/amt-2023-66
Preprint. Discussion started: 27 June 2023

Atmospheric Measurement Techniques
Discussions

Development of the MEaSUREs blue band water vapor algorithm – Towards a long-term data record

Huiqun Wang[1], Gonzalo González Abad[1], Chris Chan Miller[2], Hyeong-Ahn Kwon[3], Caroline R. Nowlan[1], Zolal Ayazpour[1,4], Heesung Chong[1], Xiong, Liu[1], Kelly Chance[1], Ewan O'Sullivan[1], Kang Sun[4], Robert Spurr[5], Robert J. Hargreaves[1]

[1] Atomic and Molecular Physics, Center for Astrophysics | Harvard & Smithsonian, Cambridge, MA, USA
[2] Department of Earth and Planetary Sciences, Harvard University, Cambridge, MA, USA
[3] Department of Environmental & Energy Engineering, University of Suwon, Gyeonggi-do, Republic of Korea
[4] Department of Civil, Structural and Environmental Engineering, University of Buffalo, Buffalo, NY, USA
[5] RT Solutions Inc., Cambridge, MA, USA

Correspondence to: Huiqun (Helen) Wang (hwang@cfa.harvard.edu)

Abstract. We report the development of an algorithm for the retrieval of Total Column Water Vapor (TCWV) from blue spectra obtained by satellite instruments such as the Ozone Monitoring Instrument (OMI). The algorithm is implemented in an automatic processing pipeline and will be used to generate a long-term data record as part of a MEaSUREs project. TCWV is calculated as the ratio between the Slant Column Density (SCD) and Air Mass Factor (AMF). Both these factors are improved upon previous work by incorporating more constraints or physical processes. For the SCD, we have optimized the retrieval window to 432 – 466 nm, performed a temperature correction, and employed a new stripe-removal post-processing routine. The use of OMI collection 4 spectra reduces the SCD fitting uncertainty by ~9% with respect to collection 3. For the AMF, we perform on-line radiative transfer using VLIDORT. Over land surfaces, we use bi-directional reflectances based on MODIS products. Over the oceans, we consider surface roughness and water-leaving radiance, and we find that water-leaving radiance is important for avoiding large TCWV biases over the oceans.

Under relatively clear conditions, the MEaSUREs OMI data are well correlated with the reference datasets, having correlation coefficients of r ~0.9. Over the oceans, MEaSUREs-AMSR_E has an overall mean (median) of ~ 1 mm (0.6 mm) with a standard deviation of σ ~6.5 mm, though large systematic differences in certain regions are also found. Over land surfaces, MEaSUREs-GPS has an overall mean (median) of -0.7 mm (-0.8 mm) with σ ~5.7 mm. Even a small amount of cloud can introduce large bias and scatter; thus, without further correction, strict data filtering criteria are required. However, the MEaSUREs TCWV data can be corrected through machine learning when accurate measurements are abundant. In this regard, under all-sky conditions, the mean bias of MEaSUREs over the oceans reduces from 4.5 mm (without correction) to -0.3 mm (with correction using LightGBM models), and the standard deviation decreases from 11.8 mm to 3.8 mm. We also examined the representation error of the GPS stations using the dense GEONET data. The within-pixel variance of TCWV varies with grid size following a power law dependence. At 0.25°×0.25° resolution, the derived representation error is about 1.4 mm.

1 Introduction

As part of a NASA's Making Earth System Data Records for Use in Research Environments (MEaSUREs) project, we are developing long-term consistent data records for formaldehyde (HCHO), glyoxal ($C_2H_2O_2$) and water vapor (H_2O) using spectra collected by several spaceborne instruments. These instruments include the Global Ozone Monitoring Experiment (GOME) [Burrows et al., 1999], Scanning Imaging spectrometer for Atmospheric CHartographY (SCHIAMACHY) [Bovensmann et al., 1999], Ozone Monitoring Instrument (OMI) [Levelt et al., 2006], GOME-2 [Munro et al., 2016], and Ozone Mapping and Profiler Suite (OMPS) [Goldberg et al., 2013]. With the exception of OMPS (which is UV only), all the other instruments measure the UV-blue wavelength range, which contains the characteristic absorption signatures of these molecules. Collectively, the resulting products will form long-term data records of HCHO, $C_2H_2O_2$ and H_2O since 1995. The OMI instrument forms the backbone of the MEaSUREs H_2O project due in part to its long-term stability and overlap with other instruments. This helps us establish a baseline towards which other products can be homogenized.

https://doi.org/10.5194/amt-2023-66
Preprint. Discussion started: 27 June 2023

Atmospheric Measurement Techniques Discussions

Total Column Water Vapor (TCWV), also known as Precipitable Water Vapor (PWV), is an essential climate variable, playing an important role in the weather and climate. TCWV datasets have been derived from a wide range of spectral regions (visible, NIR, IR, microwave, GPS) using a variety of methods. A comprehensive review of satellite water vapor retrievals can be found in Schröder et al. [2018]. As a member of the suite of molecules for the MEaSUREs project, our TCWV product not only makes a useful addition to existing water vapor datasets, but also provides insights for improving retrievals of HCHO and $C_2H_2O_2$ which are important indicators of tropospheric pollution, and which affect ozone concentration. This is because the suite of molecules is retrieved using a common processing pipeline. The availability of extensive TCWV validation data can help test this pipeline and diagnose issues that are difficult to discern from the other molecules. In addition, as NO_2 also absorbs in the visible range, we expect that lessons learned from assessing the H_2O product may be useful for NO_2 retrievals, and vice versa.

In the blue wavelength region, water vapor is a weak absorber whose characteristic spectral feature can be exploited to measure the column amount through spectral fitting. Such retrievals have been performed for OMI, GOME-2, and Sentinel-5 Precursor Tropospheric Monitoring Instrument (TROPOMI) [Wagner et al., 2013; Wang et al., 2014, 2016, 2019; Borger et al., 2020; Chan et al., 2020, 2022]. A frequently used retrieval method is to derive the Slant Column Density (SCD) from spectral fitting and convert this SCD to the Vertical Column Density (VCD) using an Air Mass Factor (AMF).

Previous studies employed a variety of algorithm configurations for SCD retrieval and AMF calculation. This paper reports the findings during the development of the MEaSUREs water vapor product. In particular, we focus on the lessons learned from the OMI TCWV through investigations of the MEaSUREs algorithm configuration. This helps guide our development of the processing pipeline to improve the overall quality of all products. Most recently, the processing pipeline was used to generate the OMPS HCHO product [Nowlan et al., 2022].

The present paper focuses mainly on the MEaSUREs H_2O algorithm applied to OMI. The long-term TCWV product will be presented in the future. Section 2 below is for the derivation of SCD, and Section 3 the calculation of AMF. Section 4 presents comparisons with reference validation datasets and provides discussions. Section 5 summarizes the results. The retrieval algorithm was derived using the OMI collection 3 spectra for 2005-2006 as it was completed before the official release of the OMI collection 4 L1b data [Kleipool et al., 2022]. As will be shown, the OMI collection 4 generally leads to better spectral fitting, thus, collection 3 presents a more rigorous test of the algorithm, processing pipeline, and data quality. Unless otherwise specified, the MEaSUREs TCWV data used in this paper were derived from the OMI collection 3 spectra.

2 Slant Column Density (SCD)

2.1 General algorithm description

The theoretical basis for our spectral fitting has been detailed elsewhere [González Abad et al., 2015, 2019; Nowlan et al., 2022]. A brief description pertinent to this paper is provided here. Observed spectral radiances within the retrieval window are directly fitted with the modeled radiances using the Levenberg-Marquart non-linear least squares minimization algorithm. The modeled spectra are based on the Beer-Lambert law for the target molecule (H_2O) and contributing molecules (O_3, NO_2, O_2-O_2, liquid water, $C_2H_2O_2$, and IO), as well as the baseline and scaling closure polynomials, the under-sampling correction [Chance et al., 2005], the Ring effect [Chance and Spurr, 1997] and the liquid water Ring effect. To account for changes in instrument calibration with time, we also fit a wavelength shift and an instrument slit function which is represented by a super-Gaussian profile characterized by an asymmetry parameter (assumed to be 0 for OMI, but may vary for other instruments), a half-width at 1/e (HW1e) parameter, and a shape parameter [Beirle et al., 2017; Sun et al., 2017; Bak et al., 2019]. Problematic spectral positions (i.e., wavelengths) flagged in the Level 1b spectra are masked out during the fitting. The fitting also employs outlier rejections for spectral positions beyond 3σ of the fitting residuals [Richter et al., 2011]. For HCHO and $C_2H_2O_2$, radiance references are usually needed to mimic the role of solar irradiance in the fitting [Chan Miller et al., 2014; Nowlan et al., 2022]. However, for water vapor, the solar irradiance measurements are used directly, because water vapor generally has stronger signal in the spectra (Section 2.3). The details of the MEaSUREs H_2O SCD algorithm are summarized in Table 1.

High-resolution reference spectra for H_2O and other molecules are convolved with the on-line derived instrument slit function, in order to fit the observed spectra. The fitting employs the latest reference spectra from the literature (Table 1). In particular, we compute the H_2O reference spectrum using HITRAN2020 [Gordon et al., 2022] which features a more complete spectral line list and improved quality compared with previous editions [Gordon et al, 2017]. For this purpose, the

https://doi.org/10.5194/amt-2023-66
Preprint. Discussion started: 27 June 2023

Atmospheric Measurement Techniques Discussions

water vapor lines are sampled every 0.0001 nm, convolved with a HW1e = 0.04 nm Gaussian function, and recorded on a 0.01 nm reference spectrum grid. This ensures an accurate representation of water vapor absorption when the reference spectrum is convolved with the instrument slit function. Due to the highly structured nature of the water vapor band, sufficiently narrow spectral sampling is required in order to avoid spectral distortion. Sparser sampling will risk missing the true amplitudes of spectral peaks which will then result in an overabundance of the retrieved water vapor because absorption cross sections would appear too low. Since the publication of HITRAN2020, several updates for the H_2O spectral lines have been made (https://hitran.org, last access Mar 27, 2023). These updates are not used for the retrievals presented here. However, we performed a sensitivity test using the updated H_2O spectral line list. Results show that the spectral updates have negligible effect on the TCWV retrieved using the algorithm summarized in Table 1, though our future retrievals will use the updated HITRAN H_2O line list.

Table 1. MEaSUREs H_2O SCD retrieval algorithm summary.

Ingredients	Details
Window	[432, 466] nm
Closure polynomials	Baseline: 3rd order Scaling: 3rd order
Calibration	wavelength shift slit function: Super-Gaussian HW1e and shape parameter k
Reference spectra	solar: [Chance and Kurucz, 2010] H_2O: HITRAN2020 [Gordon et al., 2022] (283 K) NO_2: [Vandale et al., 1998] (220 K & 294 K) O_3: [Serdyuchenko et al., 2014] (223K) O_2-O_2: [Finkenzeller and Volkamer, 2022] (293 K) $C_2H_2O_2$: [Volkamer et al., 2005] (296 K) IO: [Spietz and Burrows, 2005] liquid water (lqh2o): [Mason and Fry, 2016] Ring effect: [Chance and Spurr, 1997] water Ring (vraman): [Chance and Spurr, 1997]
Other	Under-sampling correction [Chance et al., 2005]

2.2 Temperature correction

We derived the H_2O reference spectra for a series of temperatures between 223 K and 303 K at 10 K intervals, and pressures between 0.05 atm and 1.0 atm. These reference spectra are not very sensitive to pressure for the vertical range wherein water vapor is concentrated; however, reference spectra depend significantly on temperature (Fig. A1). Using the OMI collection 3 Orbit 5108 as an example, we find that the water vapor SCDs fitted using the reference spectra at different temperatures are quite different, although they are highly correlated (Fig. 1 top row). Generally speaking, higher temperatures result in more water vapor being fitted.

We performed linear regressions between pairs of the SCDs retrieved at different H_2O reference temperatures. The results are shown in Table 2. We experimented with three other OMI orbits following the same procedure and obtained very similar results. Our default fitting algorithm uses the H_2O reference spectrum at 283 K (Table 1). After the fitting, we use Table 2 to correct the fitted SCD to a value corresponding to an effective temperature for each scene (i.e., Level 2 pixel). Specifically, we find the two closest temperatures in Table 2, calculate the corresponding SCDs using the corresponding regression lines, and obtain the corrected SCD through a linear interpolation in temperature between them. The temperature correction affects the pixels whose effective temperatures are far from the reference temperature, but it does not significantly change the histograms of the SCDs (Fig. A2).

The effective temperature for each retrieval is a vertically weighted temperature. As the AMF for each layer reflects the light path through that layer (Section 3), these box AMFs are used as weights for the corresponding temperature profile. As an example, the bottom panels of Fig. 1 show the distributions of effective temperatures for two cloud fraction ranges (f =

https://doi.org/10.5194/amt-2023-66
Preprint. Discussion started: 27 June 2023

Atmospheric Measurement Techniques
Discussions

0.0-1.0 and *f* = 0.0-0.1) on July 1, 2005. The curves show local peaks near 263 K and 283 K. Both peaks are prominent under all-sky conditions, while the 283 K peak dominates relatively clear conditions. This indicates that the 263 K peak is largely due to clouds. As we are most interested in relatively clear conditions, 283 K is used as the default in Table 1.

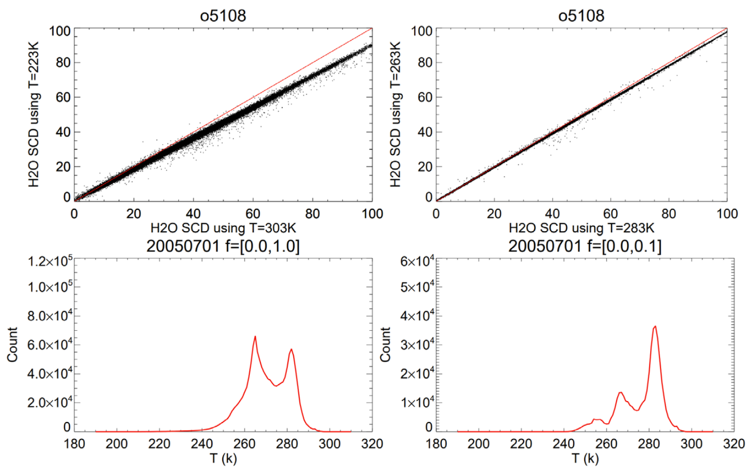

Figure 1: (Top row) Scatter plots of the fitted H_2O SCDs for OMI collection 3 Orbit 5108 (on July 1, 2005) using the H_2O reference spectra at different temperatures, (top left) 303 K versus 223 K and (top right) 283 K versus 263 K. The y=x line is plotted in red as a reference. (Bottom row) Histograms of the temperatures weighted by the box AMFs on July 1, 2005 for cloud fraction *f* within 0.0-1.0 (bottom left) and 0.0- 0.1 (bottom right).

Table 2. Linear regression results for OMI collection 3 Orbit 5108, where x is the fitted SCD using the algorithm summarized in Table 1 (*i.e.*, using 283K for water vapor), y is the fitted SCD using the same algorithm but for different temperatures for the H_2O reference spectrum. Both x and y have the unit of 10^{23} molecule/cm^2.

Temperature (K)	**Regression line**
223	y = 0.915 x + 0.012
233	y = 0.931 x + 0.010
243	y = 0.947 x + 0.008
253	y = 0.961 x + 0.006
263	y = 0.975 x + 0.004
273	y = 0.988 x + 0.002
283	y = 1.000 x + 0.000
293	y = 1.012 x - 0.002
303	y = 1.023 x - 0.003

2.3 Retrieval window optimization

In the blue wavelength range, the strongest water vapor absorption band occurs within 442.6 – 443.2 nm [Gordon et al., 2022]. This band is much weaker than the water vapor absorption in the red and longer wavelengths. However, except for very dry conditions (TCWV < 5 mm, where 1 mm = 3.34556×10^{21} molecules/cm^2), the combination of absorption cross section and atmospheric abundance makes the contributions of water vapor in satellite spectra readily differentiable from those of interference molecules and fitting residuals (Fig. A3). Thus, retrieval windows covering this characteristic spectral feature and its spectral neighborhood can generally lead to a reasonable pattern of global water vapor distribution.

However, despite the general agreement on the spatial pattern, Wang et al. [2019] found that the amount of retrieved SCD is quite sensitive to the choice of retrieval window. Previous studies employed different windows. For example, Wagner et al. [2013] used 430-450 nm for OMI and GOME-2, Wang et al. [2016] used 427.7-465.0 nm for OMI, Chan et al. [2020] used 427.7-455.0 nm for GOME-2, and Garane et al. [2023] used 435-455 nm for TROPOMI. Different retrieval windows include different amounts of information for the target molecule and interference species, and the absolute and relative importance of each component varies with the choice of retrieval window. Furthermore, the reference spectrum and other algorithm ingredients may influence the result in subtle ways. Consequently, it is best to optimize the retrieval window as part of the chosen algorithm configuration (Table 1), so that it works best for the target molecule.

Multiple factors were considered for the choice of retrieval window in Wang et al. [2019]; these include the fitting Root Mean Squared (RMS) error, the fitting uncertainty, the fraction of valid retrievals, and the retrieval window length. These diagnostics are used here, along with two additional factors - the common mode amplitude (i.e., the standard deviation of the averaged fitting residuals for each swath) and the correlation coefficients between the target and interference species. We streamlined the processing pipeline to sweep systematically through the starting and ending wavelength ranges of possible retrieval windows and collect the relevant diagnostic variables.

Figure 2 shows selected diagnostics and the corresponding SCDs retrieved using different retrieval windows for OMI collection 3 Orbit 5108. As reported in Wang et al. [2019], the fitted SCDs vary substantially with the retrieval window by as much as ~25%, and the pattern of variation is complex. The fitting uncertainty and fitting RMS generally oppose each other, suggesting that some sort of compromise is needed to optimize the window choice. This consideration points to the diagonal region of each panel; this region also happens to minimize the common mode amplitude which represents the magnitude of systematic residuals in the fit. Note, although the common mode is derived for each swath, it is not used in the fitting. Had the common mode been fitted, it would have lowered the fitting RMS without much effect on the fitted SCD [Wang et al., 2014]. As noted in Wang et al. [2019], the fraction of valid retrievals tends to be higher when the end-limit wavelength is longer than ~462 nm (not shown), which favors longer retrieval windows.

To further refine the retrieval window, we investigate the correlations between H_2O and interference molecules. Figure 3a shows the amplitude of the leading correlation coefficient (r), while Fig. 3b indicates which interference molecules are responsible for these coefficients. When the end-limit wavelength is shorter than ~468 nm, the correlation is lower (r ~0.18) and preferred. Correlation coefficients r > 0.5 can be found for longer ending wavelengths. Considering the other diagnostics above, we adopt 432 – 466 nm as the final H_2O retrieval window for MEaSUREs. In this case, the largest correlation coefficient is with O_2-O_2, and the retrieved SCD is within the middle range. The 432 – 466 nm window is also consistent with the optimization result obtained using another OMI orbit.

As a representative example, Fig. 4 shows the fitting RMS and the SCD fitting uncertainty derived from the default retrieval algorithm (Table 1) for OMI collection 3 on July 1, 2005. All the retrievals with main data quality flag (MDQF) = 0 are used in the plot. This criterion checks that the fitting has converged, the fitted SCD is < 4×10^{23} molecules/cm^2, and the SCD is positive within twice the fitting uncertainty [Wang et al., 2016]. The top panels summarize the statistics for each 5 mm SCD bin using box-and-whisker plots wherein the 10th, 25th, 50th, 75th, and 90th percentiles are indicated. The bottom panels show the overall probability distributions. The fitting RMS is mostly < 1.2×10^{-3}, with a median (mean) of 9.5×10^{-4} (1.0×10^{-3}) and a standard deviation of 4.3×10^{-4}. For SCD > 20 mm, the median RMS values are between 8.0×10^{-4} and 1.0×10^{-3}, with a local minimum around SCD = 40 mm and a local maximum around SCD = 70 mm. Smaller SCDs (<20 mm) have larger median RMS (1.0×10^{-3} – 1.2×10^{-3}), especially for SCD < 5 mm, where the diminishing H_2O signals approach the level of the fitting residuals. A similar pattern is exhibited by the SCD fitting uncertainty, which has an overall median (mean) of ~6.1 mm (6.6 mm) with a standard deviation of ~2.8 mm. For SCD > 20 mm, the median fitting uncertainty is generally < ~6 mm, with a local minimum near SCD = 40 mm. For SCD between 0 and 20 mm, the median fitting uncertainty decreases from ~7.8 mm to ~6.4 mm.

We performed a test by replacing the OMI collection 3 Level 1b spectra with collection 4, keeping everything else the same. Comparisons of the results are shown in Fig. 5. The fitted SCDs are clustered around the 1:1 line with rare outliers (Fig. 5a). For Orbit 10629, the median and mean SCDs for collection 4 (32.6 mm and 35.1 mm) remain within 0.2 mm of those for collection 3 (32.8 mm and 35.3 mm), representing a change of only ~0.6%, though the standard deviation of the differences between the results is ~3.0 mm. The fitting RMS and fitting uncertainty are generally lower for collection 4 (Fig. 5b-d). For July 15, 2006, the median fitting RMS decreases from 1.05×10^{-3} for collection 3 to $0.97\text{x}10^{-3}$ for collection 4 (corresponding to a ~8% drop), and the median fitting uncertainty decreases from 6.8 mm for collection 3 to 6.2 mm for collection 4 (a ~9% drop). This result indicates a better quality of the OMI collection 4 Level1b spectra.

https://doi.org/10.5194/amt-2023-66
Preprint. Discussion started: 27 June 2023

Atmospheric Measurement Techniques
Discussions

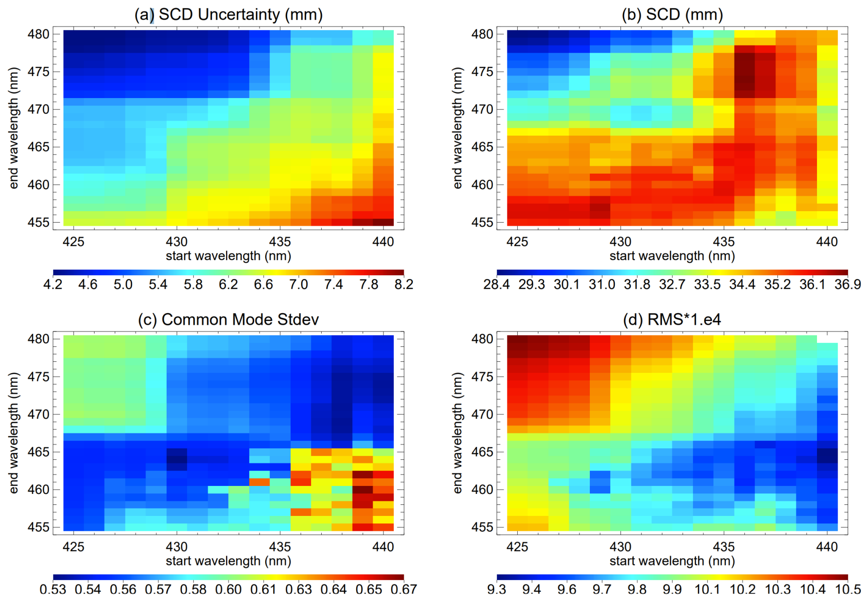

Figure 2: (Top left) Median fitting uncertainty (mm), (top right) median fitted SCD (mm), (bottom left) median standard deviation of common mode, and (bottom right) median fitting RMS×10^4 for different retrieval windows using the configuration summarized in Table 1. The retrieval windows are represented by the start wavelength on the x-axis and end wavelength on the y-axis. Results are derived from OMI collection 3 Orbit 5108.

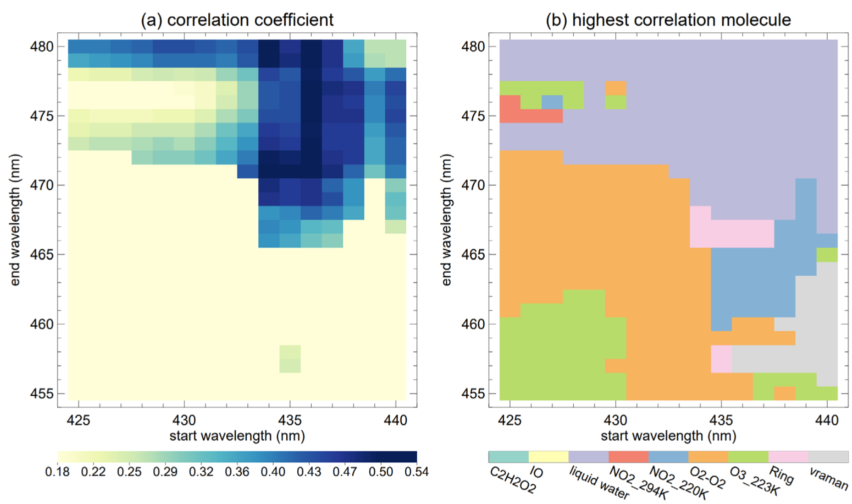

Figure 3: (Left) Leading correlation coefficients between H_2O and interference molecules for MEaSUREs spectral fitting algorithm optimization and (right) the corresponding interference molecules (See Table 1 for abbreviated names). Results are derived from OMI collection 3 Orbit 5108.

https://doi.org/10.5194/amt-2023-66
Preprint. Discussion started: 27 June 2023

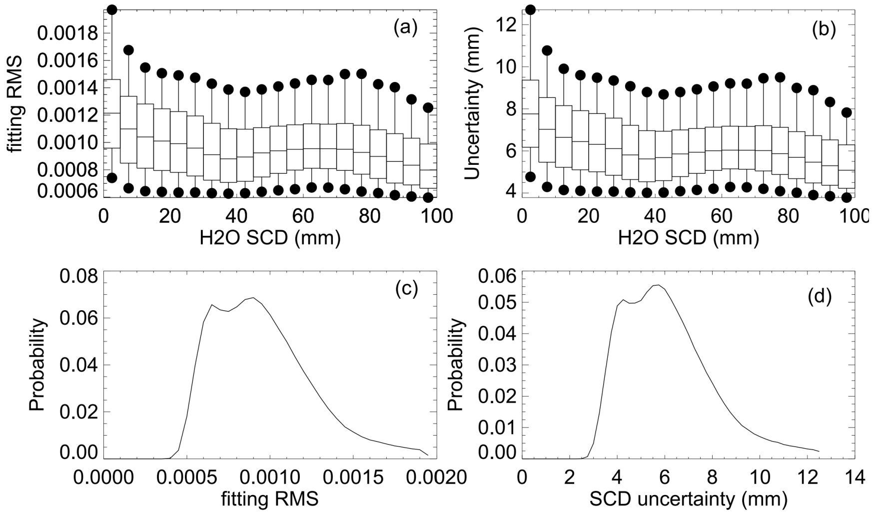

Figure 4: (a) Fitting RMS versus fitted H_2O SCD (mm); (b) SCD fitting uncertainty (mm) versus fitted SCD (mm); (c) Probability distribution of fitting RMS; (d) Probability distribution of SCD fitting uncertainty (mm). (a) and (b) are box-and-whisker plots for each 5 mm SCD bin, where the boxes denote the 25th, 50th, and 75th percentiles and the dots denote the 10th and 90th percentiles. All panels are derived from OMI collection 3 Level 1b data for July 1, 2005.

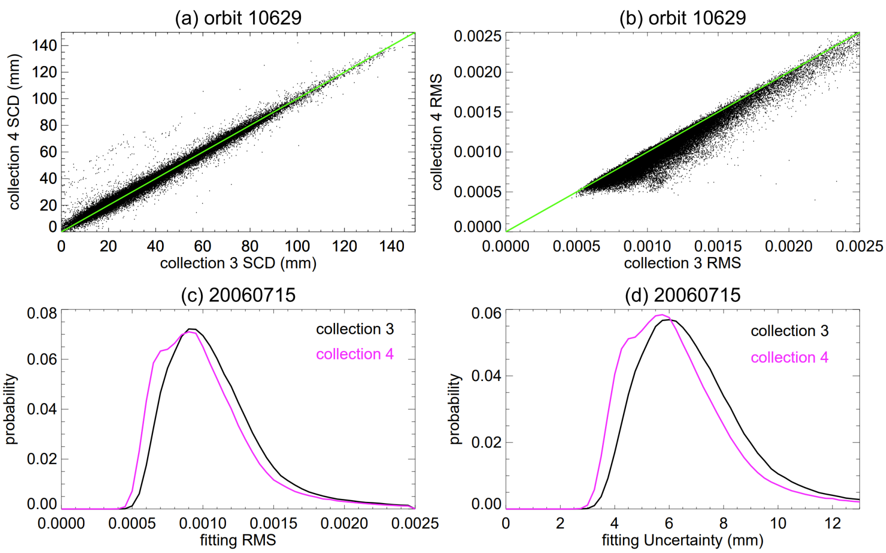

Figure 5: Comparison between OMI collection 3 and collection 4 spectral fitting results. Top panels show collection 3 versus collection 4 scatter plots of (a) fitted SCD and (b) fitting RMS for Orbit 10629 on July 15, 2006. The 1:1 line is plotted in green for reference. Bottom panels are probability distributions of (c) fitting RMS and (d) fitting uncertainty for July 15, 2006, where collection 3 is in black and collection 4 in magenta.

2.4 Stripe removal

For instruments using 2D (spectral versus spatial) detectors, such as OMI, along-track stripes in the retrieval products are common. These stripes reflect systematic differences associated with detector sensitivities. They can be smoothed by

https://doi.org/10.5194/amt-2023-66
Preprint. Discussion started: 27 June 2023

Atmospheric Measurement Techniques Discussions
Open Access
EGU

applying a correction factor for each across-track pixel position (*i.e.*, a correction vector) during post-processing [Wang et al., 2014, 2016]. Previously, a correction vector was derived for each month from the ratio between the monthly averaged SCDs at each across-track position and their 3rd order polynomial fit (as a function of across-track pixel number). The SCDs used for this purpose were filtered according to the main data quality flag, fitting RMS, and cloud fraction [Wang et al., 2016]. The smoothed SCDs can be calculated as the ratios between the unsmoothed SCDs and the corresponding correction factors. Since VCD=SCD/AMF, the correction vector can also be used to smooth the VCD. The MEaSUREs product uses the same general approach, but with the following updates.

First, we no longer use cloud filtering when we derive the correction vector. This is because the spectral fitting under cloudy conditions has comparable quality to that under relatively clear conditions; furthermore, including cloudy scenes significantly increases the sample size for statistics when fewer number of orbits are used to derive the correction vector. Figure 6 shows the statistics of the fitting RMS as a function of the fitted SCD for two cloudy scenarios using OMI collection 3 data on July 1, 2005. The RMS for cloud fraction $f > 0.8$ tends to be smaller than that for cloud fraction $f < 0.15$ due to improved signal-to-noise ratio.

Second, instead of using a fixed correction factor for each month, we derive dynamically a correction factor for each swath using its neighboring data. Stripes can sometimes pop up, disappear, and change within a short time span. As an example, the swaths in Fig. 7a are all obtained on July 12, 2015, but the details of their stripes vary. In particular, the swath covering the central Pacific (Orbit 5268) has an obvious stripe with much lower SCDs than those for other across-track positions (Fig. A4), but the stripe is not present in the other swaths. To better represent local- and time-variable behavior, we derive three versions of correction vectors using the data within 0, 1, and 7 orbits of each swath on both sides (corresponding to a total of 1, 3, and 15 orbits), respectively. These can be considered as the local, regional, and global correction vectors (Fig. A5). The three vectors are similar, but not identical. Each correction vector is used to de-stripe variables such as the SCD, temperature corrected SCD, VCD, and temperature corrected VCD. To improve robustness, the three versions of the corrected variables are averaged to get the final de-striped variables. Figure. 7b shows the corresponding de-striped SCDs. We note that the de-striping method is non-unique [Wang et al., 2016]; nonetheless, the specific method can satisfactorily remove most stripes and mitigate others.

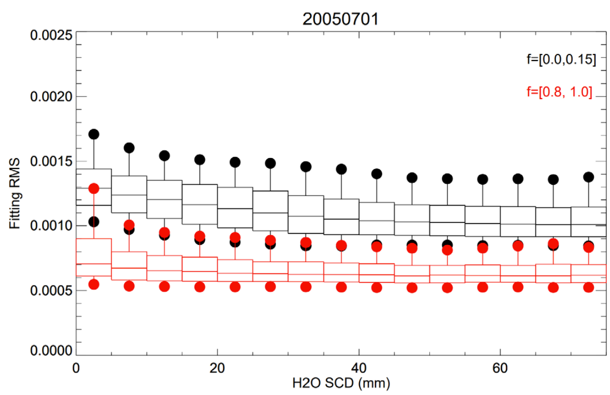

Figure 6: Fitting RMS as a function of fitted H_2O SCD (mm) for cloud fraction $f \geq 0.80$ (red) and $f \leq 0.15$ (black). Box-and-whiskers are plotted for each 5 mm SCD bin, where the boxes denote the 25th, 50th and 75th percentiles of the fitting RMS and the dots represent the 10th and 90th percentiles. Results are derived using OMI collection 3 data for July 1, 2005.

The correction vectors are derived using the following procedure. For each across-track position, we find the median SCD from the fittings that satisfy the main data quality check (MDQF=0) and possess fitting RMSs less than an empirical threshold. Note that using the median of the temperature corrected SCDs also works, as the temperature correction does not significantly affect the overall histogram distribution (Fig. A2). The RMS threshold is intended to filter out outliers. It is set to the smaller of the median + 1.5 median absolute deviation of the RMSs and an absolute maximum RMS (e.g., 5×10^{-3} for OMI). During data collection, any obviously anomalous stripes, such as the one in Orbit 5268 described above, were proactively discarded, as pixels in these stripes tend to escape the filtering criteria mentioned before. These anomalous

https://doi.org/10.5194/amt-2023-66
Preprint. Discussion started: 27 June 2023

Atmospheric Measurement Techniques Discussions
Open Access

stripes typically have median SCDs that are far less (<50%) than those for other across-track positions with a significant portion of negative values, but with seemingly normal fitting RMSs (Fig. A4). The median SCD is thus used to automatically identify the anomalous stripes. Occasionally, when reliable spectral information is missing at one or more wavelengths that can significantly influence the fitted H_2O SCD, spectral fitting still fortuitously proceeds using the remaining unmasked wavelengths and ends up with a normal fitting RMS. Although these situations are rare, they can invalidate the de-striping correction if left untreated.

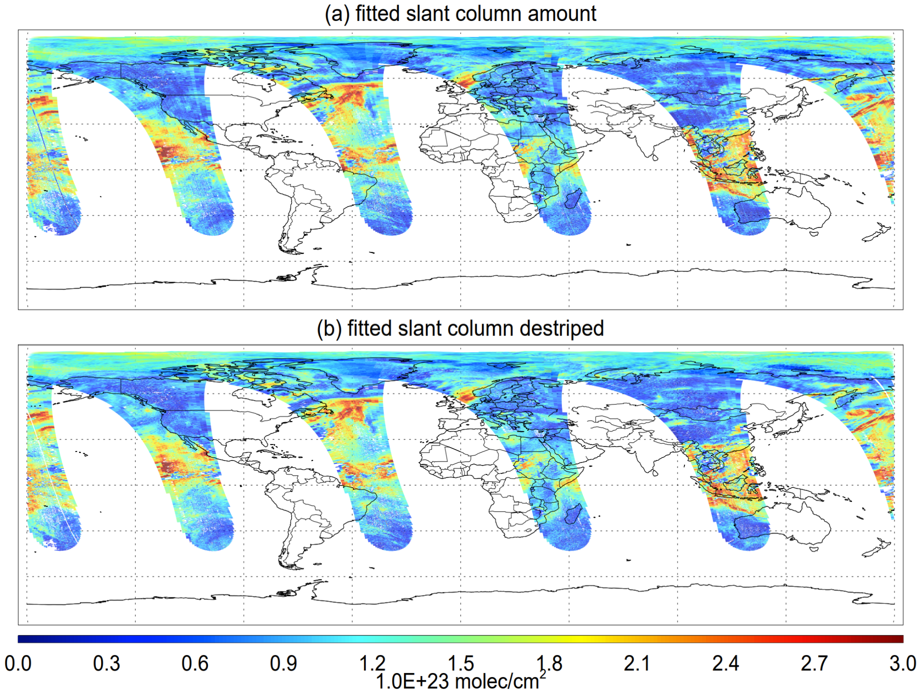

Figure 7: (a) Fitted SCD and (b) de-striped SCD for every 3rd swath (for clarity) on July 12, 2015. Results are derived from OMI collection 3 spectra. Orbit 5268 is the one covering the central Pacific and has an obviously anomalous stripe in (a) which is voided in (b). Other stripes in the swaths are removed or mitigated.

The use of the median instead of the mean of the SCDs improves the robustness of the result. The SCD median vector thus obtained is fitted with a 5th order polynomial. A reflection extension of 3 data points (5% of the 60 OMI across-track positions) on both ends of the vector is used for the fitting. We also perform a couple of iterations to reject outliers that are beyond ±20% of the fitted curve. The correction vector is obtained from the ratio between the SCD median vector and the final polynomial fit. By construction, the mean of the correction vector is very close to 1. However, the variation can be substantial. For example, the regional correction vector for OMI Orbit 5268 has a mean of 1.001, a standard deviation of 0.068, with the smallest and largest value of 0.82 and 1.19, respectively (Fig. A5). The overall level of across-track variations is comparable to that in Wang et al. [2016], though the details differ.

3 Air Mass Factor (AMF)

The AMF quantifies the light path through the atmosphere for the molecule of interest. Under the optically thin assumption, it can be calculated as the vertically integrated product of the scattering weight *W*(z) and shape factor *S*(z) [Palmer et al., 2001]. The shape factor is obtained from the normalized a priori vertical profile of water vapor partial columns. Previous studies have employed monthly climatology or statistical analyses of vertical profiles [*e.g.*, Wang et al., 2019; Chan et al., 2020]. For practical reasons, MEaSUREs retrievals use the monthly mean climatology at the local time sampled by the satellite from a 0.5°×0.5° full-physics GEOS-Chem simulation [Bey et al., 2001] for 2018. For water vapor,

https://doi.org/10.5194/amt-2023-66
Preprint. Discussion started: 27 June 2023

Atmospheric Measurement Techniques Discussions

the profiles essentially come from the Modern Era Retrospective Research and Applications Version 2 (MERRA-2, 0.5°×0.67°) data [Gelaro et al., 2017], which drives the GEOS-Chem simulation. The simulation also provides vertical profiles for temperature and other molecules that are needed for the MEaSUREs project. The MEaSUREs products provide W(z) for each scene so that users can switch to other S(z) to recalculate the corresponding AMF if desired.

The scattering weight W(z) describes the sensitivity of the Top of Atmosphere (TOA) backscattered radiance to the trace gas optical depth for atmospheric layers at different heights [Palmer et al., 2001]. It depends on the illumination and viewing geometry, surface reflectance, and atmospheric absorption and scattering associated with molecules, aerosols, and clouds. For partly cloudy scenes, the Independent Pixel Approximation (IPA) is used where the AMF is composed of a clear-sky part and an overcast-sky part weighted by the cloud radiance fraction [Martin et al., 2002]. The cloud radiance fraction (w) is related to the cloud fraction (f) through the Top of Atmosphere (TOA) radiances for clear-sky (I_{clear}) and overcast-sky (I_{cloud}) conditions ($w = fI_{cloud}/[fI_{cloud} + (1-f)I_{clear}]$) [Nowlan et al., 2022]. Most studies use pre-calculated Look-Up-Tables (LUTs) to interpolate for each scene [*e.g.*, Wang et al., 2019; Chan et al., 2020]. In this paper, we perform on-line AMF calculations for each scene using the Vector Linearized Discrete Ordinate Radiative Transfer (VLIDORT) model v2.8 [Spurr et al., 2006, 2008; Spurr and Christi, 2019] through a user-friendly interface. On-line AMF calculation avoids interpolation errors associated with the use of LUTs (which can be a few percent or more for individual scenes [Lorente et al., 2017]); more importantly, it provides the freedom to account dynamically for a wide variety of surface BRDFs, surface pressures, and other factors (e.g., aerosols). The AMF for H_2O is calculated at 442.0 nm.

The following setup was used in VLIDORT to calculate W(z), I_{clear} and I_{cloud}. The model uses 4 streams (discrete ordinates) in the polar half-space and 47 vertical layers from the surface to 0.01 hPa. Surface pressure is taken from MERRA-2 at the time of observation, with an adjustment according to the Global One-kilometer Base Elevation (GLOBE) database from NOAA. Besides Rayleigh scattering, the radiative transfer calculation considers atmospheric absorption by O_3, NO_2 and H_2O using vertical profiles from the GEOS-Chem simulation mentioned before. Clouds are assumed to be Lambertian reflectors with an albedo of 0.8. This assumption also underlies the OMCLDO2 product's cloud fraction and cloud pressure [Veefkind et al., 2016] which are inputs to the AMF calculation. Some aerosol effects are implicit in the cloud information [Boersma et al., 2004, 2011]; however, the lack of an explicit treatment of aerosols in the current pipeline may result in large biases for areas with high aerosol loading. The effects of aerosols on the AMF depend on the aerosol types and vertical profiles. Although aerosol corrections have been performed using LUTs [Kwon et al., 2017; Jung et al., 2019; Vasilkov et al., 2021], on-line radiative transfer with aerosols remains challenging, as it not only requires a large amount of a priori information for aerosol optical properties, horizontal and vertical distributions, but also comes with a high computational cost.

While the Lambertian-equivalent reflectance product OMLER [Kleipool et al., 2008] was used in previous retrievals [Wang et al., 2014, 2016, 2019], a more sophisticated surface reflectance treatment described below is implemented in the MEaSUREs pipeline. This allows us to account for the variation of surface reflectance in a more physically consistent manner. We note that OMLER was used to derive OMCLDO2; thus, the cloud information used has an inconsistency with the new surface treatment, which could result in error for cloudy scenes.

Over land surfaces, we use VLIDORT's Bidirectional Reflectance Distribution Function (BRDF) supplement. This package calculates the bi-directional reflectance using a MODIS-style combination of Ross-Thick, Li-Sparse, and Reciprocal (RTLSR) kernels. The implementation is similar to that in Qin et al. [2019] except that the kernel amplitudes are taken from the daily collection V006 MODIS BRDF product (MCD43C1) [Schaff and Wang, 2015]. The V006 product captures rapid land surface changes related to vegetation, snow, and disturbances [Wang et al., 2018]. Since 442 nm is outside the wavelengths covered by MCD43C1, we use the Zoogman et al. [2016] surface spectral model to extend the MODIS kernel amplitudes to this wavelength.

Over water, we use VLIDORT's VSLEAVE supplement for ocean optics [Spurr and Christi, 2019]. This is based on a number of sources for pure water and pigment scattering and absorption, plus semi-empirical models of marine backscatter [Morel and Maritorena, 2001; Fasnacht et al. [2019]. It considers two processes - (a) the surface roughness and glint associated with wind-driven waves and (b) water-leaving radiances due to interaction with organics in the ocean. For ocean surface roughness, we use the Cox-Munk slope distribution [Cox and Munk, 1954] driven by MERRA-2 winds at 2 m height and the monthly ocean salinity from the World Ocean Atlas 2009 [Antonov et al., 2010]. For water-leaving

https://doi.org/10.5194/amt-2023-66
Preprint. Discussion started: 27 June 2023

radiances, we estimate the effect of ocean organics using the monthly climatology of chlorophyll concentrations derived from MODIS observations [Hu et al. 2012].

Figure 8 shows histogram comparisons between the AMFs calculated using OMLER and those using the new BRDF/VSLEAVE combination, for July 1, 2005. When cloud fraction is high ($f > 0.85$), the two sets produce very similar results, as cloud scattering predominates. The histograms peak at small AMFs (<0.1) corresponding to high cloud tops (*i.e.*, low cloud top pressures). However, when cloud fraction is low ($f < 0.15$), the BRDF/VSLEAVE AMFs are apparently larger than the OMLER AMFs for both land and ocean surfaces. This implies that the new surface reflectance treatment will tend to lower the VCD for the same SCD. The BRDF land AMFs also have a wider spread in histogram distribution which probably reflects larger heterogeneities associated with geometries.

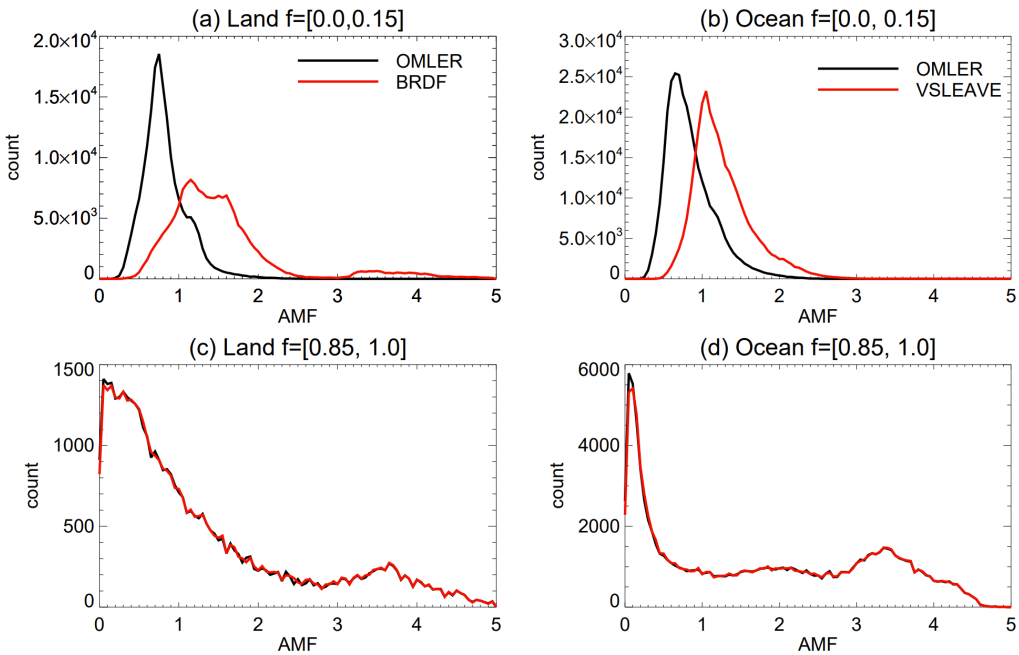

Figure 8: Histograms of AMFs on July 1, 2005, derived for (left) land surfaces and (right) ocean using (black) OMLER and (red) BRDF/VSLEAVE surface reflectance for cloud fraction (top) $f = [0.0, 0.15]$ and (bottom) $f = [0.85, 1.0]$.

Errors in AMFs mainly come from the uncertainties in the inputs to radiative transfer model, such as trace gas profile, surface albedo, cloud information, and aerosol correction [Lorente et al., 2017]. Wang et al. [2019] tested the influence of water vapor vertical profiles using the daily versus monthly MERRA-2 profiles for July 2006. They found that the resulting TCWV differs by 0.3 ± 5.0 mm. Wang et al. [2014] found a strong AMF sensitivity to surface albedo within the typical albedo range (0.05 – 0.15) for blue wavelengths. Specifically, a 0.02 increase in surface albedo corresponds to a ~9% increase in AMF. The MODIS BRDF has an RMS error < 0.0318, and a bias within ±0.0076, with needle-leaf and broad-leaf forests having negative biases and other surface types (mixed forest, savanna/shrubland, grass/cropland/tundra, and desert) having positive biases [Wang et al., 2018]. Clouds are a major source of error for trace gas retrievals. Even for relatively small cloud fractions between 0.1 and 0.2, Lorente et al. [2017] found that the AMFs for NO_2 can change by 20 – 40%, which also applies to H_2O. Wang et al. [2014] found that as the cloud pressure increases from 850 hPa to 900 hPa, the AMF for H_2O increases from 1.6 to 2.0 (a 25% change) for a typical observation scenario. For the OMCLDO2 product, the precision of cloud fraction f is generally better than 0.01, the precision of cloud pressure is ~25 hPa for $f < 0.10$ and ~10 hPa for $f > 0.50$ [Veefkind et al., 2016]. For the TCWV discussed here, the overall AMF uncertainty is estimated to be 10 – 20% for relatively clear ($f < 0.10$) conditions and much larger for cloudier conditions. While error propagation provides a

https://doi.org/10.5194/amt-2023-66
Preprint. Discussion started: 27 June 2023

uncertainty estimate, it usually does not include all error sources. Comparison with well-established highly accurate data provides a more concrete error estimate which will be presented next.

4. Comparisons and Discussions

To evaluate the MEaSUREs TCWV, we compare with high fidelity reference datasets. Over the oceans, we use the daily 0.25°×0.25° Advanced Microwave Scanning Radiometer AMSR_E data derived by the Remote Sensing Systems (RSS) using their Version 7 algorithm [Wentz et al., 2014]. AMSR_E on the Aqua platform observes at approximately the same local time (1:30 PM) as OMI on the Aura satellite. The data are available from 2002 to 2011. Microwave observations can penetrate through clouds and are considered to be among the best over the ice-free ocean under non-precipitating conditions. The accuracy of AMSR_E TCWV is about 1 mm [Wentz et al., 2005; Mears et al., 2015].

Over land surfaces, we compare with the GPS TCWV data [Wang et al., 2007] downloaded from the University Corporation for Atmospheric Research (UCAR) website. The dataset has an accuracy of better than ~1.5 mm and is available 2-hourly for all weather conditions [Wang et al., 2007]. The data comprise measurements from the International GNSS Service (IGS) network (1995-2012) and the GEONET network (1997-2005). The IGS stations are scattered around the globe and are most abundant in North America and Europe (Fig. A6a). In this paper, the IGS data are used for the overall evaluation of the MEaSUREs retrievals over land. GEONET is the nationwide GPS array of Japan; consisting of ~1200 GPS stations with an average spacing of ~20 km (Fig. A6b), it is the largest national GPS network in the world. In this paper, the GEONET data are used to assess the representation error of station observations to gain a better understanding of the satellite validation results.

4.1 Comparison for the Ocean

To make a direct comparison with the AMSR_E data which are available only over the oceans [Wentz et al., 2005], we generate the daily Level 3 MEaSUREs TCWV product at the same spatial resolution (0.25°×0.25°). This grid size is about twice the OMI Level 2 pixel size (13 km × 24 km). The Level 3 gridding program performs tessellation for the variables of interest based on the pixel areas and SCD fitting uncertainties of the Level 2 data. Before gridding, we filter the MEaSUREs Level 2 de-striped and temperature corrected VCDs using the standard criteria (i.e., MDQF = 0, cloud fraction $f < 0.05$, cloud pressure > 500 hPa, AMF within 0.25 – 4.0, and fitting RMS < 0.0012). These criteria are the default for all the Level 3 data discussed in this paper unless specified otherwise. After gridding, we compare the daily coincident AMSR_E and MEaSUREs data for the pixels without precipitation, snow, or ice.

Figure 9 shows the results for July 2005 and January 2006, with the MEaSUREs TCWV data derived from the OMI collection 3 spectra. There are over 2 million data points used for each panel. The datasets cluster around the 1:1 line in the 2D joint histogram distributions, suggesting an overall good agreement. For July 2005, the linear correlation coefficient is $r = 0.89$ and the TCWV difference (Δ=MEaSUREs - AMSR_E) has a mean of 1.1 mm, a median of 0.65 mm, and a standard deviation of $\sigma = 6.6$ mm; For January 2006, the corresponding values are $r = 0.90$, mean $\Delta = 1.0$ mm, median $\Delta = 0.5$ mm, and $\sigma = 6.3$ mm. When using the MEaSUREs TCWV data derived from the OMI collection 4 spectra for July 2005, we find $r = 0.90$, mean $\Delta = 1.28$ mm, median $\Delta = 0.75$ mm, and $\sigma = 6.4$ mm. These statistics are similar to those when the OMI collection 3 spectra were used, despite that the spectral fitting for OMI collection 4 is better (Fig. 5). This suggests that the AMF is a significant source of error for the MEaSUREs OMI TCWV.

Previously, Wang et al. [2019]'s OMI versus SSMIS comparison for $f < 0.05$ in July 2006 showed a mean bias $\Delta = 0$ mm, but a slightly larger $\sigma = 7.1$ mm and lower correlation coefficient $r = 0.82$. It is worth noting that although the level of difference with respect to the reference datasets is comparable between this paper and other studies [Wang et al., 2019; Chan et al., 2020; Garane et al., 2023], the retrieval configurations are different. The SCDs and AMFs for MEaSUREs result from more optimization constraints and physical processes. As the MEaSUREs AMFs are generally larger than those calculated with OMLER under relatively clear conditions (Fig. 8ab), the Wang et al. [2019] algorithm probably has low biases in both the AMFs and SCDs that compensate each other.

One physical process important for the MEaSUREs TCWV product is the water leaving radiance handled in VLIDORT's VSLEAVE package (Section 3). Figure 10 shows the histograms of the MEaSUREs - AMSR_E differences for July 2005, where the OMI collection 3 spectra were used for MEaSUREs. The red line corresponds to the result for the MEaSUREs retrieval with nominal AMF calculation, illustrating a satisfactory agreement with the reference dataset. The

https://doi.org/10.5194/amt-2023-66
Preprint. Discussion started: 27 June 2023

black line is derived from a sensitivity test where the MEaSUREs TCWV uses the AMF calculated over the oceans with the Cox-Munk function only. In this sensitivity test, the radiation has no water-leaving component, resulting in larger AMFs, and consequently the VCDs in the sensitivity test are too low (by more than 5 mm) compared with those from AMSR_E. As organics in the water are even more important for the UV reflectance [Fewell et al., 2019], the water leaving radiance is also expected to influence molecules retrieved from the UV wavelength range, such as HCHO and O_3. However, Rayleigh scattering is stronger in the UV, and the net effect for UV molecules awaits further investigation.

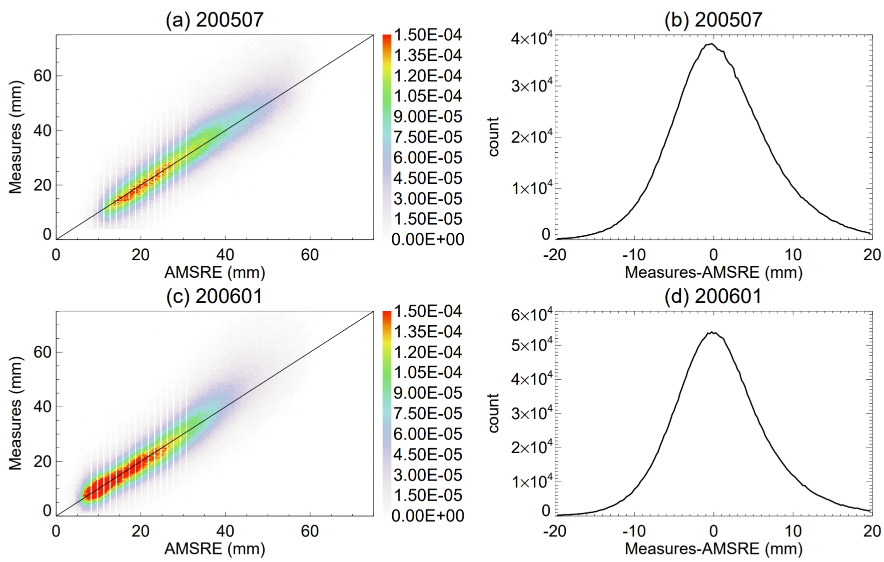

Figure 9: TCWV (mm) comparisons between MEaSUREs and AMSR_E using daily coincident data for (top) July 2005 and (bottom) January 2006. MEaSUREs TCWV data were derived from the OMI collection 3 spectra. Left panels are 2D probability distributions. The y=x line is plotted for reference. Right panels are histograms of the MEaSUREs - AMSR_E difference (mm).

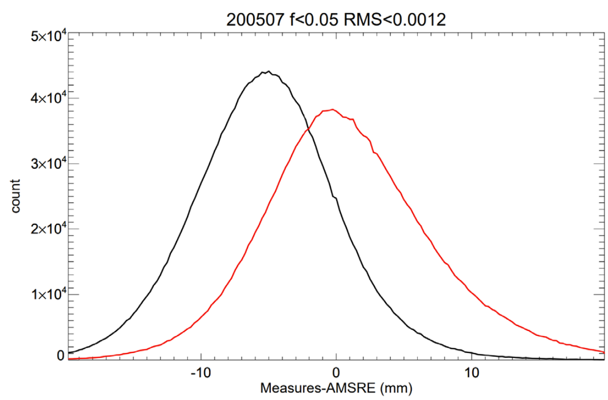

Figure 10: Histograms of MEaSUREs - AMSR_E for July 2005. The MEaSUREs data were retrieved from the OMI collection 3 spectra and the standard data filtering criteria were employed during Level 3 gridding. The black line is for the TCWV differences when the AMF is calculated using the Cox-Munk function only in a MEaSUREs sensitivity test, whereas the red line is for the differences when the nominal AMF calculation is used for MEaSUREs.

The left panels of Figure 11 show the statistics of the MEaSUREs - AMSR_E differences for each 5 mm TCWV bin for July 2005. The same data as those for Fig. 9ab are used here. The absolute values of the median and mean differences are mostly below 1 mm. The largest deviation of ~1.5 mm occurs for the 35 – 40 mm TCWV bin. The inter-quartile ranges vary roughly within ±5 mm. The relative median and mean differences are small (< ~4%) for TCWV>15 mm.

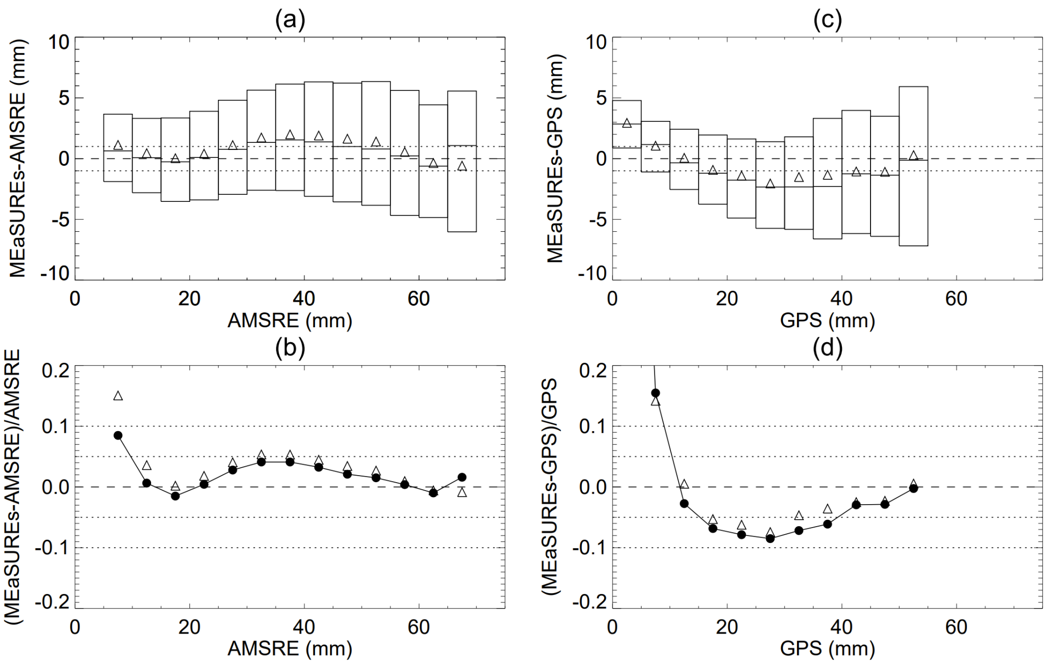

Figure 11: (Top) Absolute and (bottom) relative differences between MEaSUREs data and reference data for each 5 mm TCWV bin. Each box in the top row indicates the 25th and 75th percentiles for the bin. The line and triangle within each box represent the 50th percentile and mean, respectively. Each dot (triangle) in the bottom panels indicates the median (mean) difference divided by the TCWV of the bin. Left panels are derived using MEaSUREs (OMI collection 3) and AMSR-E data for July 2005. Right panels are derived using MEaSUREs (OMI collection 3) and GPS data for July 2005, Jan 2006, and July 2006. Dashed and dotted lines are guidelines for ease of visualization.

However, the comparison results are highly dependent upon clouds. As shown in Fig. A7, a slight increase in cloud fraction from $f < 0.05$ to $f < 0.15$ results in MEaSUREs overestimation beyond +1.5 mm for TCWV between 35 and 65 mm. Relaxing the cloud pressure criterion to include all clouds has a similar effect. As a consequence, compounding the effects of cloud fraction and cloud pressure lead to significant positive bias and large scatter. For example, with $f < 0.15$ and all cloud pressures, the MEaSUREs TCWV is larger than that for AMSR_E by ~4 mm for the 55 – 60 mm bin. The high sensitivity to cloudy scenes highlights the necessity to use strict cloud filtering for validation, which is why we employed the default standard filtering criteria described before. It also suggests that, when cloud fractions $f > \sim 0.1$ are used, the overall mean or median of the difference may be misleading, since positive bias due to clouds can disguise negative bias associated with other parts of the retrieval. Thus, data with significant cloud contamination are not recommended for use without further correction.

To evaluate whether the MEaSUREs - AMSR_E TCWV has any regional dependence, we examine the time mean of the daily differences for summer and winter months in Fig. 12cd. The panels are generated by averaging the daily MEaSUREs - AMSR_E maps for each 2-month period, with the requirement that at least 14 days of data are available for each grid square. The daily differences are produced in the same manner as those in Fig. 9. The result remain essentially the same when the OMI collection 4 spectra are used instead of collection 3. Figure 12 shows non-uniform spatial distribution for the differences. In northern summer, the region near the maritime continent in the Indian ocean has a

https://doi.org/10.5194/amt-2023-66
Preprint. Discussion started: 27 June 2023

Atmospheric Measurement Techniques
Open Access
Discussions

positive bias of up to ~8 mm for MEaSUREs. In northern winter, significant positive bias for MEaSUREs is seen in the south Pacific at low latitudes and negative bias further south, positive bias is also seen in the Atlantic slightly north of the equator. The monthly chlorophyll climatology used in the AMF calculation may have large errors in certain regions [Fasnacht et al., 2019], and its influence on TCWV requires further investigation. As the large absolute differences occur in regions where water vapor is relatively abundant (see Fig. 12ab for context), the relative mean differences are still confined within ~5% (Fig. 11b).

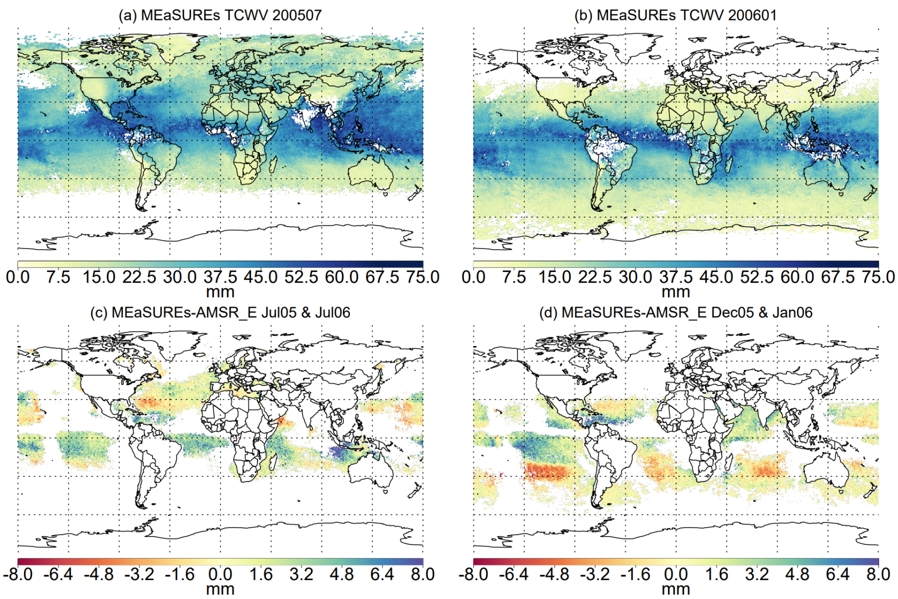

Figure 12: (Top) Monthly mean TCWV (mm) for (a) July 2005 and (b) Jan 2006 generated from the daily Level 3 MEaSUREs (OMI collection 3) data. The standard data filtering criteria are used for Level 3 gridding. (Bottom) Mean difference of MEaSUREs (OMI collection 3) - AMSR_E TCWV (mm) for (c) Jul 2005 and Jul 2006 and (d) Dec 2005 and Jan 2006.

4.1.1 Correction for all-sky TCWV over the oceans

As discussed above, although MEaSUREs and AMSR_E generally agree well under clear conditions, even a small amount of cloud can lead to large scatter and significant positive bias for the MEaSUREs data. This is despite the fact that the SCD fitting for cloudy scenes has comparable or even better fitting RMS. To expand the usability range for the MEaSUREs retrievals, we experimented with a few machine learning models to perform bias correction. These models are trained using LightGBM regression with different feature sets and architectures, where LightGBM is a gradient-boosting algorithm based on the decision tree framework and grows trees leaf-wise [Ke et al., 2017].

To demonstrate feasibility, we use 5 days in July 2005 (1^{st}, 7^{th}, 14^{th}, 21^{st}, 28^{th}) for model training and validation. We find the locations with both MEaSUREs(OMI collection 3) and AMSR_E data, with the latter being the target for learning. To save computer memory, we randomly select ~850,000 data points from the data and split them into the training and validation set using a 4:1 ratio. For each data point, we employ two sets of features selected from the variables used in MEaSUREs retrievals. Feature set 1 includes the VCD, AMF, latitude, longitude, cos(solar zenith angle), cos(viewing zenith angle), relative azimuth angle, surface pressure, surface albedo, cloud fraction, cloud pressure, temperature and water vapor mixing ratio at 27 vertical levels. Feature set 2 replaces the VCD with the SCD and replaces the temperature profile with the scattering weights. We vary the model architecture by changing the number of leaves and maximum depth of the trees for LightGBM.

The training curves and feature rankings for three models are shown in Fig. A8. Model 1 and Model 2 employ feature set 1, while Model 3 employs feature set 2. Model 1 and Model 3 use 50 leaves with a maximum depth of 150, while Model 2 uses 150 leaves with a maximum depth of 50. For all three models, the training and validation RMSE track each other well, and both drop significantly after initial oscillations. However, the feature rankings are different. The top four features in order of importance for Model 1 are VCD, cloud fraction, AMF, and longitude; those for Model 2 are cloud fraction, VCD, longitude, and surface pressure; and those for Model 3 are SCD, AMF, longitude, and water vapor mixing ratio at the surface. The variables within each feature sets are not independent, and the models use different strategies to come up with their predictions. There appears to be a tendency for models with larger maximum depth to have a sharper drop in feature importance. Conceptually, these models rely heavily on a few features to make their predictions. In comparison, the model with more leaves and shallower depth (Model 2) bases its predictions on more features whose importance declines more slowly.

Table 3. Statistics for all-sky comparisons between various TCWV data and the AMSR_E data for July 2 – 6, 2005, where Δ denotes the difference with respect to AMSR_E.

All-sky	Feature Set	Leaves/Depth	Mean(Δ) (mm)	Median(Δ) (mm)	σ(Δ) (mm)	Correlation coefficient r
MEaSUREs	-	-	4.9	2.1	11.8	0.828
Model 1	1	50 / 150	-0.42	-0.31	3.75	0.965
Model 2	1	150 / 50	-0.42	-0.32	3.85	0.963
Model 3	2	50 / 150	-0.39	-0.26	3.73	0.966

Despite the differences among the LightGBM models, they lead to similar results, as shown by the 2D joint density plots (Fig. A9). These plots are generated using the data for all cloud fractions between July 2 and July 6, 2005. Note, these dates were not used during the LightGBM training. The linear correlation coefficient between MEaSUREs and AMSR_E is r = 0.828, and the difference Δ = MEaSUREs - AMSR_E has a mean (median) of 4.9 mm (2.1 mm) with a standard deviation σ = 11.8 mm, reflecting the adverse effect of clouds. In comparison, all the LightGBM predictions agree much better with the AMSR_E data, with r ~ 0.96, mean (median) Δ < 0.5 mm, and σ ~ 3.8 mm (Table 3). Thus, with abundant reliable reference data over the oceans, there are multiple ways to improve the MEaSUREs cloudy data through bias corrections. Figure A10 shows the TCWV maps for July 4, 2005 as an example. The locations where the MEaSUREs data have large overestimates are associated with the clouds in the ITCZ and extra-tropical weather systems. The LightGBM predictions in these regions match the AMSR_E data better.

4.2. Comparison for Land Surfaces

We use the same MEaSUREs daily Level 3 product as described at the beginning of Section 4.1 (*i.e.*, using the standard filtering criteria and OMI collection 3 spectra) for validation over land surfaces. To compare with the GPS data of the IGS network [Wang et al., 2007], we use the stations whose elevations are within 250 meters of the MEaSUREs (0.25°×0.25°) gridded terrain height. For each station, we average the GPS data between 1 PM and 2 PM local time on each day. The GPS data are paired with the daily MEaSUREs Level 3 TCWV at the grid box where the station is located. To increase the sample size, we combine the data for July 2005, Jan 2006, and July 2006, resulting in more than 4,300 data pairs at over 240 IGS stations.

Figure 13 shows that the MEaSUREs data compare well with the GPS data under relatively clear conditions, with a linear correlation coefficient r = 0.89. Overall, the MEaSUREs - GPS data have a mean of -0.7 mm, a median of -0.8 mm, and a standard deviation σ of 5.7 mm. For MEaSUREs (OMI collection 4), the corresponding statistics are r = 0.90, mean (median) bias = -0.5 (-0.6), and σ = 5.8 mm. The right panels of Fig. 11 show the details of the absolute and relative differences using the statistics for each 5 mm TCWV bin. The MEaSUREs data tend to overestimate when TCWV < 10 mm and underestimate when TCWV is between 15 mm and 50 mm. The median discrepancies vary between +2.9 mm and -2.3 mm among the TCWV bins, and the inter-quartile ranges vary between 3.9 mm and 10.1 mm (Fig. 11c). The relative differences (Fig. 11d) are larger than those over the ocean, approaching -9% for the 25 – 30 mm bin, though smaller differences can be found for other bins. The larger discrepancies over land shown in Fig. 11 are concealed in the overall statistics (Fig. 13) due to positive and negative bias cancellation.

https://doi.org/10.5194/amt-2023-66
Preprint. Discussion started: 27 June 2023

Atmospheric Measurement Techniques Discussions

Systematic AMF uncertainty is one possible reason for the negative bias over land for moderate amount of TCWV. Indeed, most IGS sites are located over surface types for which the MODIS BRDF has a positive bias (compare Fig. A6a with Fig. 4 of Wang et al. [2018]). Higher surface albedo tends to increase AMF and decrease VCD. The effects of aerosols are more difficult to ascertain, as they can either increase or decrease AMF [Jung et al., 2019].

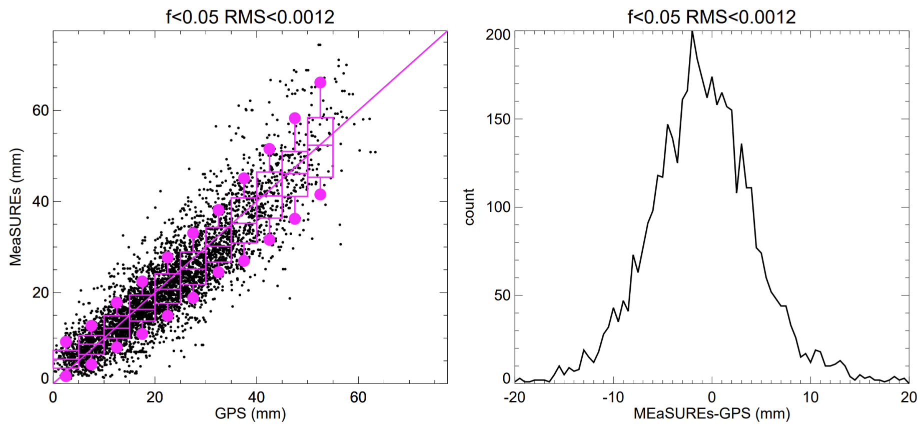

Figure 13: Comparison between MEaSUREs (OMI collection 3) and IGS TCWV (mm) for collocated data for July 2005, Jan 2006, and Jul 2006. The left panel shows the scatter plot with superimposed box-and-whisker type plots (indicating the 10th, 25th, 50th, 75th, and 90th percentiles). The 1:1 line is plotted for reference. The right panel shows the overall histogram of the (MEaSUREs - GPS) TCWV (mm).

4.2.1. GPS station representation error

Unlike the AMSR-E gridded data, GPS measurements are at individual sites. Since the Level 2 and Level 3 satellite data are associated with certain pixel areas, some differences between the GPS and satellite observations are attributable to the representation error of the station sites. Representation error is distinct from measurement error and depends on spatial resolution. The dense GEONET network (Fig. A6b) provides an opportunity to quantify the representation error of TCWV. The GEONET sites are distributed among inland, coastal, and island areas, representing diverse surface, optical, topographic, and meteorological conditions. The heterogeneity is intrinsic in the sub-pixel variations of satellite data. We estimate the spatial representation error of the GPS TCWV data by examining the variations of multi-site observations within grid squares of different sizes, following the procedure outlined below.

We divide the GEONET stations into different latitude – longitude grids of varying sizes ranging from 0.25° to 2.25° with an increment of 0.25°. At each grid square on each day, when observations from multiple stations are present within the relevant local time range, we first find the local time average for each station, then for all stations, we calculate the mean and the deviations from this mean. We assemble the deviations from all available grid squares from 2003 to 2005 and analyze their statistics. Results are shown in Fig. 14. For consistency with the criteria used in Fig. 13, we have excluded those grid squares within which the maximum inter-station altitude difference max(dz) is larger than 500 meters; however, we have included all hours of day in order to increase the sample size. Including all stations and/or constraining to a narrower local time range slightly alters the details of the plot but does not change the main conclusion. The probability distributions of within-pixel deviations roughly follow Gaussian shapes centered at zero, with sharper peaks (i.e., larger amplitude and smaller spread) for smaller grid sizes (Fig. 14a). The width of each probability curve provides a statistical measure of the TCWV variability for the corresponding grid resolution and is quantified using the standard deviation (σ) of the samples. The within-pixel TCWV standard deviation σ increases from ~1.4 mm at 0.25° to ~3.2 mm at 2.25° (Fig. 14b).

The variance $y = \sigma^2$ can be approximated using a power law relationship $y = a \cdot x^b$, where x is the grid size in angular degree, and a and b are parameters to be fitted. For the data shown in Fig. 14, a=6.228 and b=0.66. The square root of the fitted curve is overplotted in Fig. 14b. Including the grid squares with max(dz) > 500 meters leads to values of a =

https://doi.org/10.5194/amt-2023-66
Preprint. Discussion started: 27 June 2023

6.640 and b = 0.58. It is noted that the value of b = 0.66 is close to the power of the water vapor structure function found in some aircraft observations and high-resolution modeling studies under convective conditions [Fischer et al., 2013; Thompson et al., 2021]. At 0.25°×0.25° resolution, the sub-grid scale TCWV standard deviation is σ~1.4 mm. In comparison, the overall median (MEaSUREs-GPS) is -0.8 mm (Fig. 13). However, a few TCWV bins (e.g., 0 – 5 mm, 25 – 30 mm, and 30 – 35 mm, Fig. 11c) have mean (MEaSUREs – GPS) beyond this value. As the MEaSUREs project will retrieve TCWV from instruments with different ground pixel sizes, characterization of the GPS stations' representation errors helps guide our understanding of the validation results.

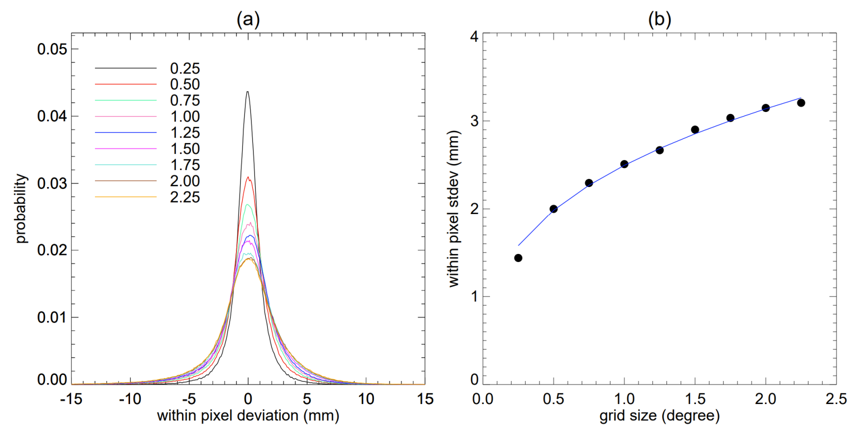

Figure 14: Within-pixel variations for different grid sizes derived from GEONET TCWV data from 2003 to 2005. Data for all local times are included. Grid squares with station elevation differences > 500 meters are filtered out. (a) Probability distributions of the within pixel TCWV deviations from the corresponding mean values. The color scheme indicates different grid sizes. (b) Standard deviations (mm) of the within-pixel deviations as a function of pixel size (degrees) are plotted as circles. The curve shows the square root of the fitted power law for the corresponding variances.

5 Summary

The TCWV retrieval algorithm for the MEaSUREs project is described in this paper. The retrieval follows the usual two-step approach to derive VCD from the ratio of SCD and AMF. As the biases and errors in SCD and AMF can sometimes compensate each other, the MEaSUREs algorithm strives to achieve satisfactory results through improvements in both these components. Hence, instead of directly transferring previous algorithms to this project, we have undertaken new optimizations and developments. The retrieval algorithm and processing pipeline developed for the MEaSUREs project will be used to generate a long-term blue band TCWV dataset.

For SCD, we have incorporated the latest reference spectra and made sure that we have sufficient spectral sampling before instrument slit function convolution. Coarse sampling will misrepresent the spectral peaks and lead to over-abundant water vapor estimates. As the fitted SCDs can vary by as much as ~25% depending on the bounds of the fitting window, we have considered additional constraints. Specifically, besides the fitting RMS, fitting uncertainty, and convergence rate, we have also considered systematic structures in the fitting residual and correlations with interference molecules. The resulting optimized retrieval window for H_2O is 432 – 466 nm. We have derived the relationships between the SCDs fitted using the H_2O reference spectrum at 283 K and those fitted at other temperatures and used these results to perform temperature corrections. We have also improved the de-striping program to better account for the variations on short time scales. For collection 3 OMI Level 1b data on July 1, 2005, the median fitting RMS is ~9.5×10^{-4} and the median fitting uncertainty is ~6.1 mm. The collection 4 OMI spectra lead to an ~9% improvement in the SCD fitting uncertainty.

We perform on-line radiative transfer (using VLIDORT v2.8) to calculate the AMF for each scene. In place of the OMLER, over land, we employ the MODIS BRDF, and over the oceans, we use the Cox-Munk roughness and calculate the water-leaving radiance. The latter is important for avoiding large under-estimates of TCWV. Cloud information from

https://doi.org/10.5194/amt-2023-66
Preprint. Discussion started: 27 June 2023

Atmospheric Measurement Techniques
Discussions

the OMCLDO2 product is used to calculate the AMFs. Aerosols are currently not treated explicitly in the on-line radiative transfer calculation.

Overall, the MEaSUREs TCWV data compare well with the reference datasets under relatively clear conditions. For July 2005, with the standard filtering criteria, we found that MEaSUREs (OMI collection 3) - AMSR_E has a mean (median) of 1.1 mm (0.6 mm) with a standard deviation of σ = 6.6 mm and a linear correlation coefficient of r = 0.89. Similar results are obtained when OMI collection 4 spectra were used for MEaSUREs TCWV. The r and σ values are better than those in Wang et al. [2019], though the bias is slightly larger. The relative mean difference between MEaSUREs and AMSR_E is < 5% for TCWV > 10 mm. Despite the overall good agreement, biases exceeding 6 mm are found in certain regions over the oceans.

Even a small amount of cloud can introduce large bias and scatter. We thus recommend using the strict data filtering criteria (Section 4.1) for MEaSUREs TCWV. To extend the usability range of the MEaSUREs data to all sky conditions over the oceans, machine learning models are employed to significantly reduce the bias to a few tenths of a mm with a σ of ~3.8 mm.

Over land surfaces, MEaSUREs - GPS has an overall mean (median) of -0.7 mm (-0.8 mm) with a σ = 5.7 mm (r = 0.89) under relatively clear conditions. However, for different TCWV bins, mean positive biases of 1 – 3 mm are seen for TCWV < 10 mm and mean negative biases of 0 – 2 mm for TCWV > 10 mm.

Representation errors for GPS stations were investigated using the dense GEONET observations. The within-pixel inter-station TCWV variance increases with grid size and can be described using a power law. At 0.25° × 0.25° resolution, the representation error (in terms of the standard deviation) is about 1.4 mm.

Appendix A.

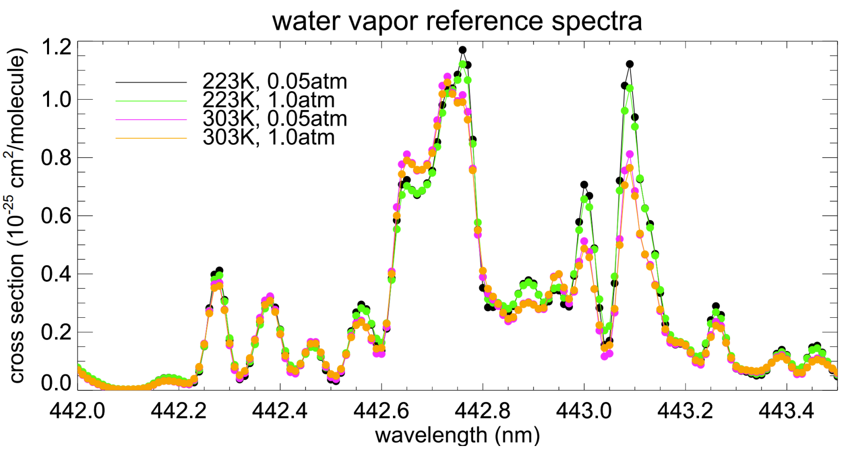

Fig. A1. Water vapor reference spectra (using the HITRAN2020 line list, see Section 2.1) near the strongest H_2O absorption feature within the blue wavelength region, plotted for different temperatures (223 K and 303 K) and pressure levels (0.05 atm and 1.0 atm). Spectral shapes are noticeably different between 223 K and 303 K. Within each temperature group, the change with pressure is relatively minor.

https://doi.org/10.5194/amt-2023-66
Preprint. Discussion started: 27 June 2023

Atmospheric Measurement Techniques
Discussions

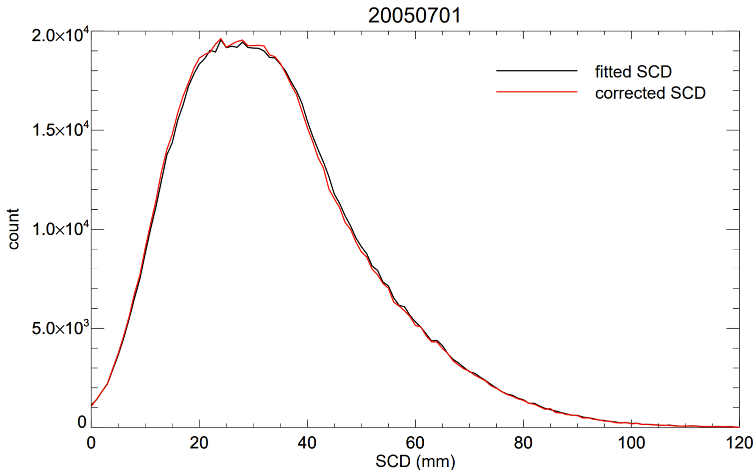

Fig. A2. Histogram of (black) fitted SCD and (red) temperature corrected SCD derived from OMI collection 3 swaths for July 1, 2005.

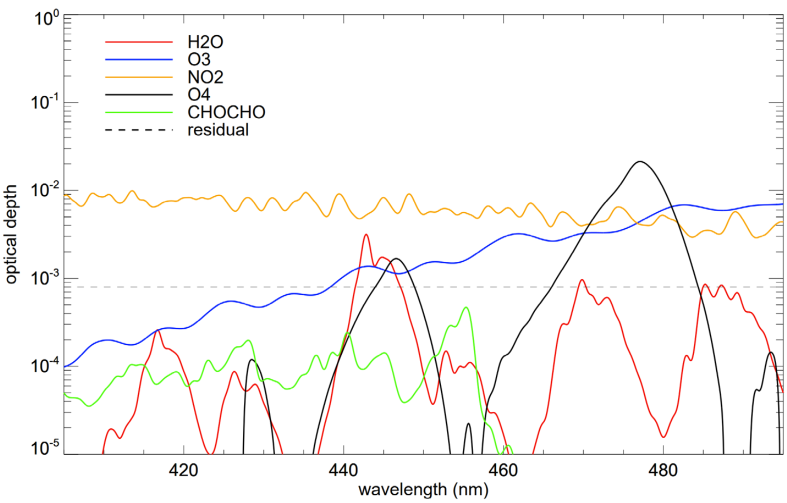

Fig. A3. Typical optical depths of absorbing molecules (colored solid lines) in the 400 – 500 nm wavelength range; the typical OMI collection 3 fitting residual level is indicated by the dashed horizontal line. Results are convolved using a Gaussian kernel with a half width at half maximum of 0.5 nm and plotted in log scale. The plot is generated using 300 Dobson Units (DU, where 1 DU = 2.6867×10^{16} molecules/cm^2) of O_3, 1.34×10^{16} molecules/cm^2 of NO_2, 1.0×10^{23} molecule/cm^2 of H_2O, 3.3×10^{43} molecule^2/cm^5 of O_4, and 1.0×10^{15} molecule/cm^2 of CHOCHO.

Atmospheric Measurement Techniques Discussions
Open Access
EGU

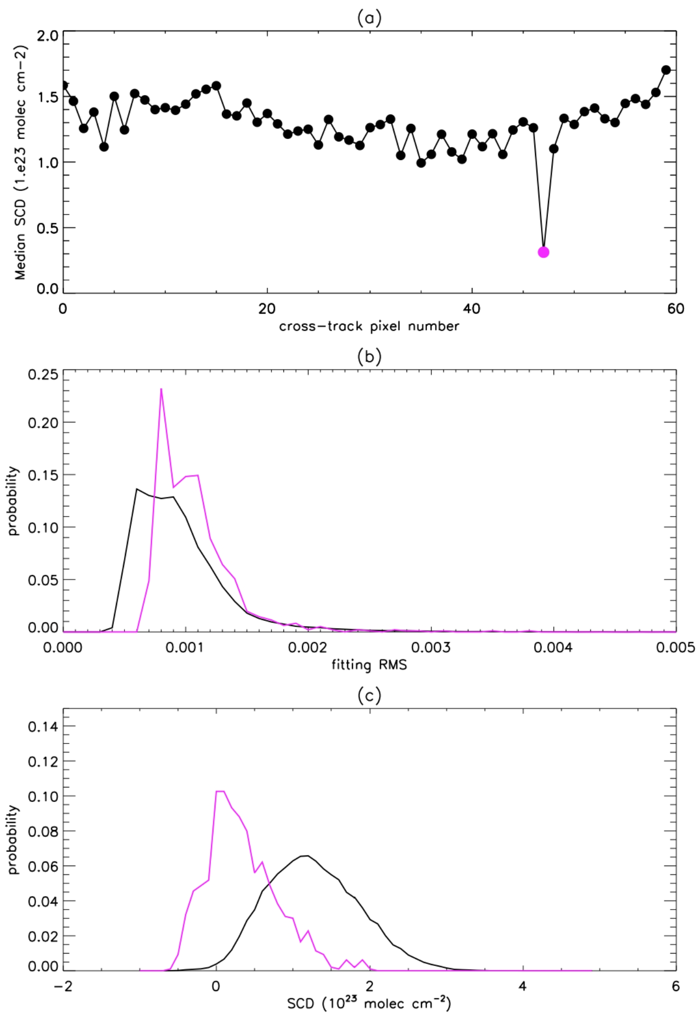

Fig. A4. (a) Median SCD for each across-track position for OMI collection 3 Orbit 5268. All data used have main data quality flag MDQF = 0 and fitting RMS < 5×10^{-3}. The magenta dot highlights the obviously anomalous across-track pixel (position number 47) for the swath. (b) Probability distributions of fitting RMSs for (black) all pixels and (magenta) pixels along across-track position number 47 of Orbit 5268. (c) Probability distributions of fitted SCDs (10^{23} molecules/cm^2) for (black) all pixels and (magenta) pixels along across-track position number 47 of Orbit 5268.

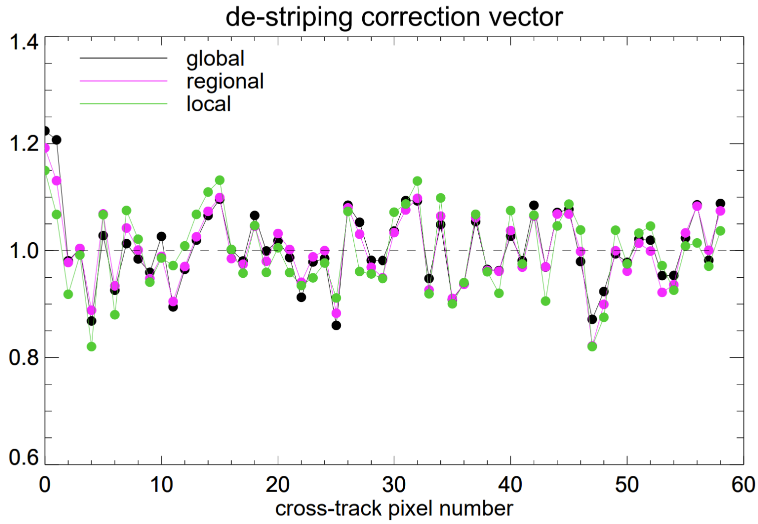

Fig. A5. The global (black), regional (magenta), and local (green) de-striping correction vectors for OMI collection 3 Orbit 5268.

https://doi.org/10.5194/amt-2023-66
Preprint. Discussion started: 27 June 2023

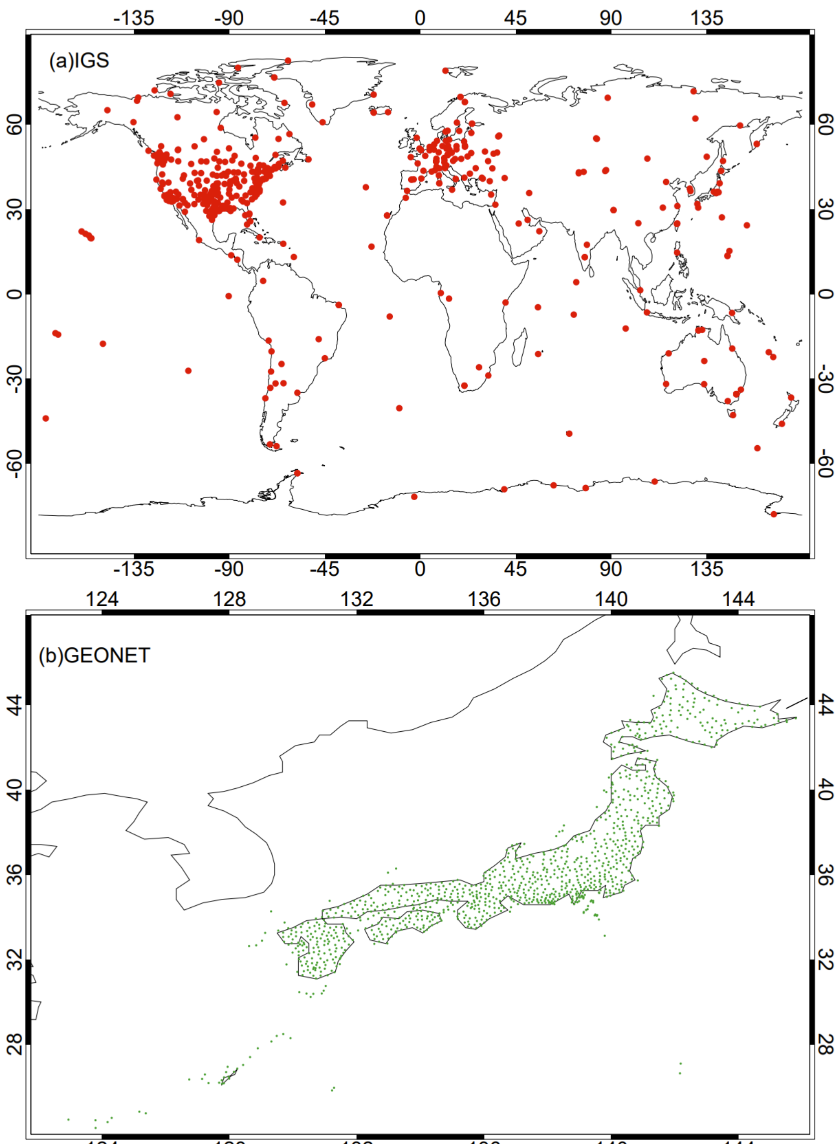

Fig. A6. GPS station locations in 2005 for the TCWV dataset [Wang et al., 2007] for the (a) IGS and (b) GEONET network. Longitudes and latitudes are indicated along the horizontal and vertical axis of each map.

https://doi.org/10.5194/amt-2023-66
Preprint. Discussion started: 27 June 2023

Atmospheric Measurement Techniques Discussions

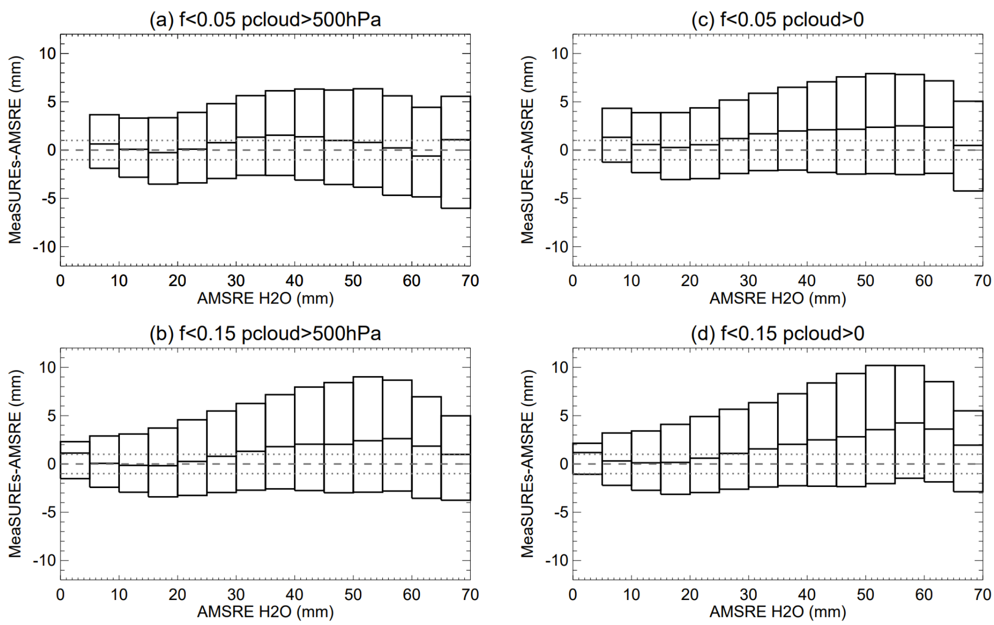

Fig. A7. Statistical distributions of 25th, 50th, and 75th percentiles of Δ = MEaSUREs (OMI collection 3) - AMSRE for each 5 mm TCWV bin in July 2005. The MEaSUREs Level 3 daily products for all panels use the usual MDQF=0 and RMS < 0.0012 criteria except for cloud fraction (*f*) and cloud pressure (pcloud) – (a) *f* < 0.05, pcloud > 500 hPa; (b) *f* < 0.15, pcloud > 500hPa; (c) *f* < 0.05, pcloud > 0; (d) *f* < 0.15, pcloud > 0.

https://doi.org/10.5194/amt-2023-66
Preprint. Discussion started: 27 June 2023

Atmospheric Measurement Techniques
Open Access
Discussions

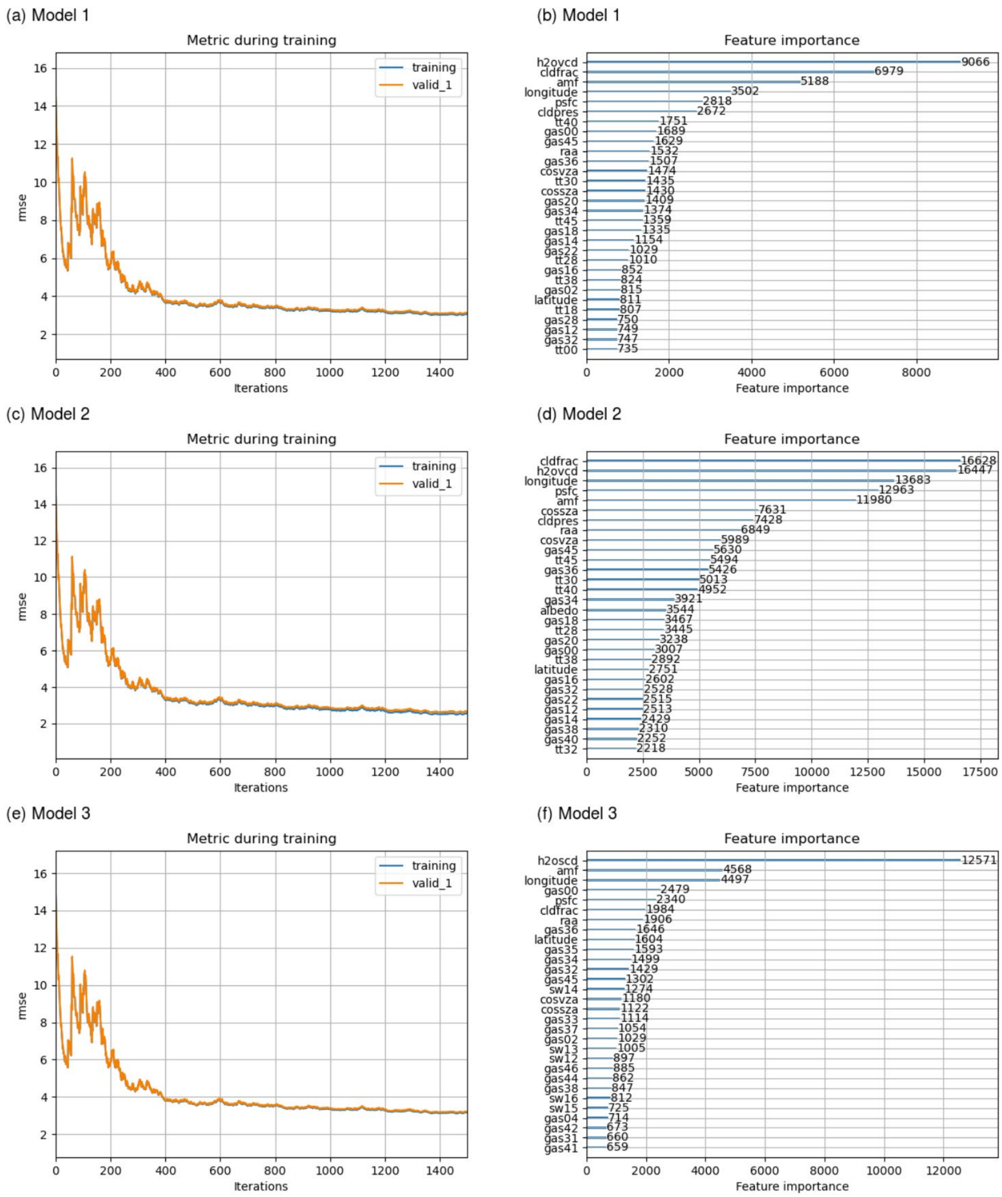

Fig. A8. (Left) Training and validation curves and (right) feature rankings for LightGBM (top) Model 1, (middle) Model 2 and (bottom) Model 3. Model 1 and Model 3 use 50 leaves with a maximum depth of 150. Model 2 uses 150 leaves with a maximum depth of 50. Model 1 and Model 2 use feature set 1. Model 3 uses feature set 2. The feature name abbreviations in the right panels are listed in Table A1.

Atmospheric Measurement Techniques Discussions

Table A1. Feature name abbreviations for the right panels of Fig. A8.

Feature name abbreviation	Meaning
h2ovcd	MEaSUREs de-striped and temperature corrected vertical column density
h2oscd	MEaSUREs de-striped and temperature corrected slant column density
amf	Air Mass Factor (AMF)
cldfrac	cloud fraction used in AMF calculation
cldpress	cloud pressure used in AMF calculation
raa	relative azimuth angle
cossza	Cosine of solar zenith angle
cosvza	Cosine of viewing zenith angle
gasXX	water vapor mixing ratio at vertical model Level XX
ttXX	temperature at vertical model Level XX
swXX	scatting weight at vertical model Level XX
psfc	surface pressure

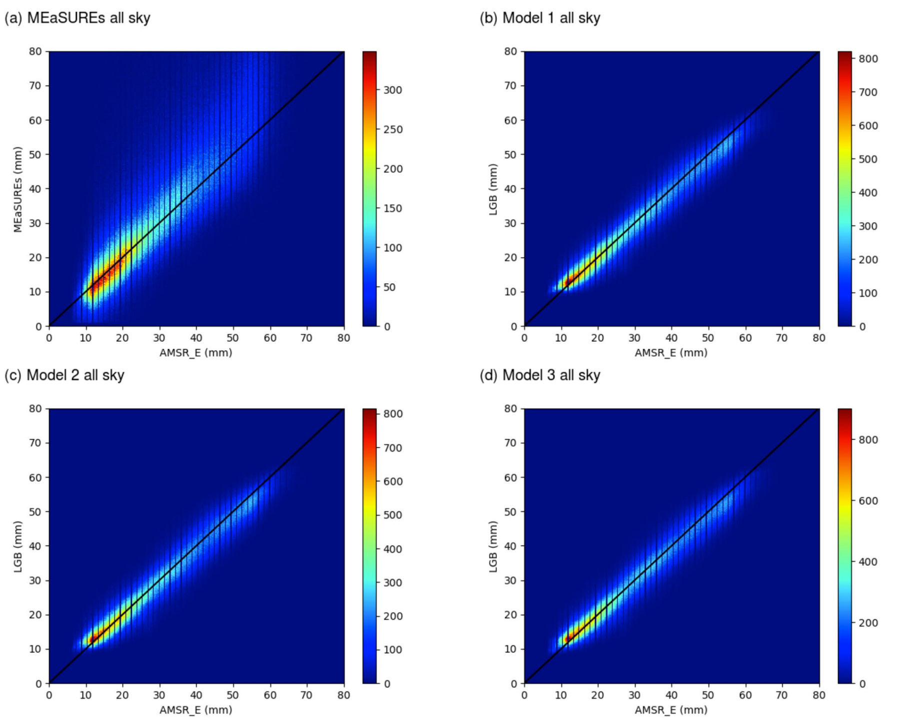

Figure A9. Joint density plot between AMSR_E TCWV and (a) MEaSUREs (OMI collection 3), (b) Model 1, (c) Model 2, (d) Model 3 for the time period from July 2 to July 6 of 2005. The color bars represent the number of data points are individually stretched.

https://doi.org/10.5194/amt-2023-66
Preprint. Discussion started: 27 June 2023

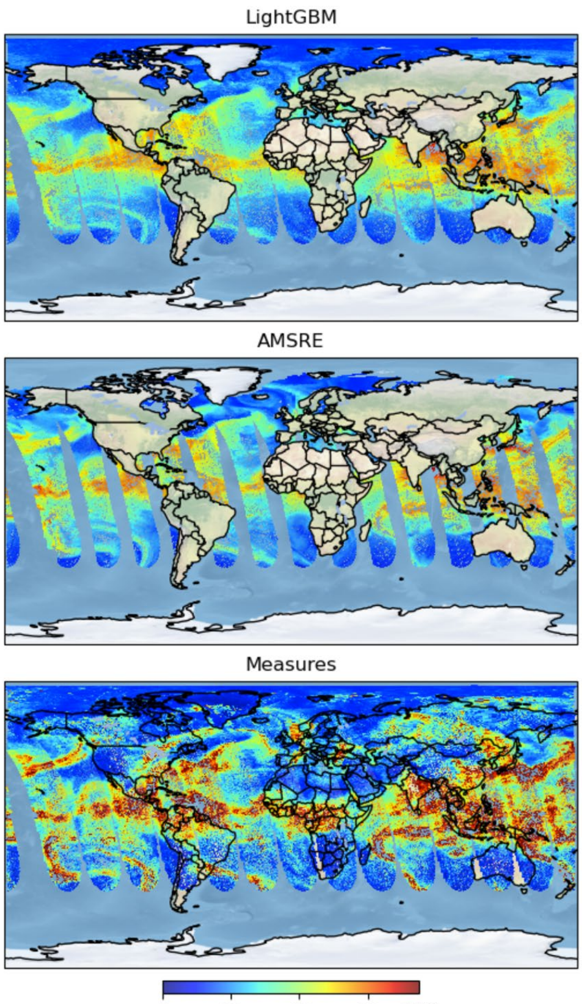

Fig. A10. TCWV (mm) map for July 4, 2005 derived from (top) LightGBM Model 1, (middle) AMSR_E, and (bottom) MEaSUREs (OMI collection 3). The background color filling for land and ocean follows the default behavior of python cartopy package with stock_img enabled [Cartopy].

Data availability

The MEaSUREs data used in this paper are available on Zenodo [Wang et al., 2023].

Author contribution

HW: conceptualization, data curation, formal analysis, funding acquisition, investigation, methodology, software, validation, visualization, writing original draft; GGA: conceptualization, funding acquisition, methodology, project administration, resources, software, supervision, review & editing; CCM: softwaree; HK: software, review & editing; CN: software, review & editing; ZA: software; HC: software, review & editing; XL: funding acquisition, review & editing; KC: funding acquisition, resources; EO: software, review & editing; KS: software, review & editing; RS: software, review & editing; RH: software, review & editing.

Competing interests

The authors declare that they have no conflict of interest.

Acknowledgement

We appreciate the support from the NASA MEaSUREs program Grant #80NSSC18M0091 and the NASA OMI core science team Grant #80NSSC21K0177. We thank Dr. Iouli Gordon for discussions on the HITRAN database. Computations for this paper were conducted on the Smithsonian High Performance Cluster (SI/HPC), Smithsonian Institution (https://doi.org/10.25572/SIHPC). The AMSR data are produced by Remote Sensing Systems and were sponsored by the NASA AMSR_E Science Team and the NASA Earth Science MEaSUREs Program. Data are available at www.remss.com. The GPS data for IGS and GEONET are downloaded from UCAR (https://eol.ucar.edu/field_projects/gps-pw). The LightGBM package is available at github.com/Microsoft/LightGBM. The cartopy package is available at https://scitools.org.uk/cartopy.

References

Antonov, J. I., Seidov, D., Boyer, T. P., Locarnini, R. A., Mishonov, A. V., Garcia, H. E., et al.: World ocean atlas 2009, volume 2: Salinity (Vol. NOAA Atlas NESDIS 69; S. Levitus, Ed.). Washington, D.C.: U.S. Government Printing Office, 2010.

Bak, J., Liu, X., Sun, K., Chance, K., Kim, J.: Linearization of the effect of slit function changes for improving Ozone Monitoring Instrument ozone profile retrievals, Atmos. Meas. Tech., 12, 3777-3788, https://doi.org/10.5194/amt-12-3777-2019, 2019.

Beirle, S., Lampel, J., Lerot, C., Sihler, H., Wagner, T.: Parameterizing the instrumental spectral response function and its changes by a super-Gaussian and its derivatives, Atmos. Meas. Tech., 10, 2, 581-598, https://doi.org/10.5194/amt-10-581-2017, 2017.

Bey, I., Jacob, D. J., Yantosca, R. M., Logan, J. A., Field, B. D., Fiore, A. M., et al.: Global modeling of tropospheric chemistry with assimilated meteorology: Model description and evaluation, J. Geophys. Res. – Atmos., 106(D19), 23073-23095. https://doi.org/10.1029/2001JD000807, 2001.

Boersma, K. F., Eskes, H. J., Brinksma, E. J.: Error analysis for tropospheric NO2 retrieval from space, J. Geophys. Res. – Atmos., 109 (D4), D04311, https://doi.org/10.1029/2003JD003962, 2004.

Boersma, K. F., Eskes, H. J., Dirksen, R. J., van der A, R. J., Veefkind, J. P., Stammes, P., et al.: An improved tropospheric NO2 column retrieval algorithm for the Ozone Monitoring Instrument, Atmos. Meas. Tech., 4 (9), 1905-1928, https://doi.org/10.5194/amt-4-1905-2011, 2011.

Borger, C., Beirle, S., Dorner, S., Sihler, H., and Wagner, T.: Total column water vapour retrieval from S-5P/TROPOMI in the visible blue spectral range, Atmos. Meas. Tech., 13, 2751-2783, https://doi.org/10.5194/amt-13-2751-2020, 2020.

Bovensmann, H., Burrows, J. P., Buchwitz, M., Frerick, K., Noel, S., Rozanov, V. V., Chance, K., Goede, A. P. H.: SCIAMACHY: Mission objectives and measurement modes, J. Atmos. Sci., 56 (2), 127-150, https:/doi.org/10.1175/1520-0469(1999)056<0127:SAOAMM>2.0.CO;2, 1999.

Burrows, J. P., Weber, M., Buchwitz, M., Rozanov, V., Ladstatter-Weissenmayer, A., Richter, A., DeBeek, R., Hoogen, R., Bramstedt, K., Eichmann, K. U., Eisinger, M.: The Global Ozone Monitoring Experiment (GOME): Mission concept and first scientific results, J. Atmos. Sci., 56, 151-175, https://doi.org/10.1175/1520-0469(1999)056<0151:TGOMEG>2.0.CO;2, 1999.

Cartopy. Met Office. git@github.com:SciTools/cartopy.git. 2015-02-18. 7b2242e.

Chan, K. L., Valks, P., Slijkhuis, S., Kohler, C., and Loyola, D.: Total column water vapor retrieval for Global Ozone Monitoring Experiment-2 (GOME-2) visible blue observations, Atmos. Meas. Tech., 13 (8), 4169-4193, https://doi.org/10.5194/amt-13-4169-2020, 2020.

Chan, K. L., Xu, J., Slijkhuis, S., Valks, P., Loyola, D.: TROPOspheric Monitoring Instrument observations of total column water vapour: Algorithm and validation, Science of the Total Environment, 821, Art. No. 153232, https://doi.org/10.1016/j.scitotenv,2022.153232, 2022.

Chan Miller, C., González Abad, G., Wang, H., Liu, X., Kurosu, T., Jacob, D. J., and Chance, K.: Glyoxal retrieval from the Ozone Monitoring Instrument, Atmos. Meas. Tech., 7, 3891-3907, https://doi.org/10.5194/amt-7-3891-2014, 2014.

Chance, K. and Spurr, R. J. D.: Ring effect studies: Rayleigh scattering, including molecular parameters for rotational raman scattering and the Fraunhofer spectrum, Applied Optics, 36 (21), 5224-5230, https://doi.org/10.1364/AO.36.005224, 1997.

Chance, K., Kurosu, T. P., Sioris, C. E.: Undersampling correction for array detector-based satellite spectrometers, Applied Optices, 44 (7), 1296-1304, https://doi.org/10.1364/AO.44.001296, 2005.

Chance, K. and Kurucz, R. L.: An improved high-resolution solar reference spectrum for Earth's atmosphere measurements in the ultraviolet, visible, and near infrared, J. Quantitative Spectroscopy and Radiative Transfer, 111 (9), 1289-1295, https://doi.org/10.1016/j.jqsrt.2010.01.036, 2010.

Cox, C., & Munk, W.: Measurement of the roughness of the sea surface from photographs of the Sun's glitter, Journal of the Optical Society of America, 44(11), 838-850, https://doi.org/10.1364/JOSA.44.000838, 1954.

Fasnacht, Z., Vasilkov, A., Haffner, D., Qin, W., Joiner, J., Krotkov, N., Sayer, A. M., and Spurr, R.: A geometry-dependent surface Lambertian-equivalent reflectivity product for UV-Vis retrievals – Part 2: Evaluation over open ocean, Atmos. Meas. Tech., 12, 6749-6769, https://doi:10.5194/amt-6749-2019, 2019.

Fewell, M. P. and von Trojan, A.: Absorption of light by water in the region of high transparency: recommended values for photon-transport calculations, Applied Optics, 58, 9, 2408-2421, https://doi.org/1559-128X/19/092408-14, 2019.

Finkenzeller, H. and Volkamer, R.: O2-O2 CIA in the gas phase: Cross-section of weak bands, and continuum absorption between 297-500 nm, J. Quantitative Spectroscopy and Radiative Transfer, 279, 108063, https://doi.org/10.1016/j.jqsrt.2021.108063, 2022.

Fischer, L., Craig, G. C., and Kiemle, C.: Horizontal structure function and vertical correlation analysis of mesoscale water vapor variability observed by airborne lidar, J. Geophys. Res., 118, 7579-7590, https://doi.org/10.1002/jgrd.50588, 2013.

Garane, K., Chan, K. L., Koukouli, M. E., Loyola, D., Balis, D.: TROPOMI/S5P total column water vapor validation against AERONET ground-based measurements, Atmos. Meas. Tech., 16, 1, 57-74, https://doi:10.5194/amt-16-57-2023, 2023.

Gelaro, R., McCarty, W., Su´arez, M. J., Todling, R., Molod, A., Takacs, L., et al.: The Modern-Era Retrospective Analysis for Research and Applications, Version 2 (MERRA-2), Journal of Climate, 30(14), 5419-5454. https://doi.org/10.1175/JCLI-D-16-0758.1, 2017.

Goldberg, M. D., Kilcoyne, H., Cikanek, H., and Mehta, A.: Joint Polar Satellite System: The United States next generation civilian polar-orbiting environmental satellite system, J. Geophys. Res. Atmospheres, 118 (24), 13,463-13,475, https://doi.org/10.1002/2013JD020389, 2013.

González Abad, G., Liu, X., Chance, K., Wang, H., Kurosu, T. P. and Suleiman, R.: Updated Smithsonian Astrophysical Observatory Ozone Monitoring Instrument (SAO OMI) formaldehyde retrieval, Atmos. Meas. Tech., 8, 19-32, https://doi.org/10.5194/amt-8-19-2015, 2015.

González Abad, G., Souri, A. H., Bak, J., Chance, K., Flynn, L. E., Krotkov, N. A., Lamsal, L., Li., C., Liu, X., Chan Miller, C., Nowlan, C. R., Suleiman, R., and Wang, H.: Five decades observing Earth's atmosphere trace gases using ultraviolet and visible backscatter solar radiation from space, J. Quant. Spectro. Radiative Transfer, 238, https://doi:10.1016/j.jqsrt.2019/04/030, 2019.

Gordan, I. E., Rothman, L. S., Hill, C., Kochanov, R. V., Tan, Y., Bernath, P. F., Birk, M., Boudon, V., Campargue, A., Chance, K. V., et al.: The HITRAN2016 molecular spectroscopic database. J. Quantitative Spectroscopy & Radiative Transfer, 203, 3-69, https://doi.org/10.1016/j.jqsrt.2017.06.038, 2016.

Gordan, I. E., Rothman, L. S., Hargreaves, R. J., Hashemi, R., Karlovets, E. V., Skinner, F. M., Conway, E. K., Hill, C., Kochanov, R. V., Tan, Y., et al.: The HITRAN2020 molecular spectroscopic database. J. Quantitative Spectroscopy & Radiative Transfer, 277, https://doi.org/10.1016/j.jqsrt.2021.107949, 2022.

Hu, C., Lee, Z., and Franz, B.: Chlorophyll algorithms for oligotrophic oceans: A novel approach based on three-band reflectance difference, J. Geophys. Res., 117, C01011, https://doi.org/10.1029/2011JC007395, 2012.

Jung, Y., González Abad, G., Nowlan, C. R., Chance, K., Liu, X., Torres, O., and Ahn, C.: Explicit aerosol correction of OMI formaldehyde retrievals. Earth and Space Science, 6 (11), 2087-2105, https://doi.org/10.5194/amt-5-529-2012, 2019.

Kleipool, Q. L., Dobber, M. R., de Hann, J. F., and Levelt, P. F.: Earth surface reflectance climatology from 3 years of OMI data, J. Geophys. Res., 113, D18308, https://doi.org/10.1029/2008JD010290, 2008.

https://doi.org/10.5194/amt-2023-66
Preprint. Discussion started: 27 June 2023

Atmospheric Measurement Techniques
Discussions

Kleipool. Q., Rozemeijer, M., van Hoek, M., Leloux, J., Loots, E., Ludewig, A., van der Plas, E., Adrichem, D., Harel, R., Spronk, S., ter Lindsen, M., Jaross, G., Haffner, D., Veefkind, P., Levelt, P. F.: Ozone Monitoring Instrument (OMI) collection 4: establishing a 17-year long series of detrended level-1b data, Atmos. Meas. Tech., 15, 3527-3553, https://doi.org/10.5194/amt-15-3527-2022, 2022.

Ke, G., Meng, Qi, Finley, T., Wang, T., Chen, W., Ma, W., Ye, Q., Liu, T.-Y.: LightGBM: A highly efficient gradient boosting decision tree, Advances in neural information processing systems, 30 (NIPS 2017), edited by Guyon, I., Luxburg, U. V., Bengio, S., Wallach, H., Fergus, R., Vishwanathan, S., Garnett, R., pp. 3149-3157, 2017.

Kwon, H.-A., Park, R. J., Jeong, J. I., Lee, S., González Abad, G., Kurosu, T. P., Palmer, P. I., and Chance, K. (2017): Sensitivity of formaldehyde (HCHO) column measurements from a geostationary satellite to temporal variation of the air mass factor in East Asia. Atmos, Chem. Phys., 17, 4673-4686, https://doi.org/10.5194/acp-17-4673-2017, 2017.

Levelt, P. F., van den Oord, G. H., Dobber, M. R., Malkki, A., Visser, H., de Vries, J., Stammes, P., Lundell, J. O. and Saari, H.: The ozone monitoring instrument, IEEE T. Geosci. & Remote Sensing, 44, 5, 1093-1101, https://doi.org/10.1109/TGRS.2006.872333, 2006.

Lorente, A., Boersma, K. F., Yu, H., Dorner, S., Hillboll, A., Richter, A., Liu, M., Lamsal, L. N., Barkley, M., De Smedt, I., Van Roozendael, M., Wang, Y., Wagner, T., Beirle, S., Lin, J., Krotkov, N., Stammes, P., Wang, P., Eskes, H. J. and Krol, M.: Structural uncertainty in air mass factor calculation for NO2 and HCHO satellite retrievals, Atmos. Meas. Tech., 10, 759-782, https://doi.org/10.5194/amt-10-759-2017, 2017.

Martin, R. V., Chance, K., Jacob, D. J., Kurosu, T. P., Spurr, R. J. D., Bucsela, E., Gleason, J. F., Palmer, P. I., Bey, I., Fiore, A. M., Li, Q. B., Yantosca, R. M., Koelemeijer, R. B. A.: An improved retrieval of tropospheric nitrogen dioxide from GOME, J. Geophys. Res. – Atmos., 107, D20, 4437, https://doi.org/10.1029/2001JD001027, 2002.

Mason, J. D., Cone, M. T. and Fry, E. S.: Ultraviolet (250-550 nm) absorption spectrum of pure water, Applied optics, 55, No. 25, 7163-7172, https://doi.org/10.1364/AO.55.007163, 2016.

Mears, C. A., Wang, J., Smith, D. and Wentz, F. J.: Intercomparison of total precipitable water measurements made by satellite-borne microwave radiometers and ground-based GPS instruments, J. Geophys. Res.- Atmos., 120, 2492-2504, https://doi.org/10.1002/2014JD022694, 2015.

Morel, A., and Maritorena, S.: Bio-optical properties of oceanic waters: A reappraisal, J. Geophys. Res., 106 (C4), 7163–7180, https://doi.org/10.1029/2000JC000319, 2001.

Munro, R., Lang, R., Klaes, D., Poli, G., Retscher, C., Lindstrot, R., Huckle, R., Lacan, A., Grzegorski, M., Holdack, A., Kokhanovsky, A., Livschitz, J., and Eisinger, M.: The GOME-2 instrument on the Metop series of satellites: instrument design, calibration, and Level 1 data processing – an overview. Atmos. Meas. Tech., 9, 1279-1301, https://doi.org/10.5194/amt-9-1279-2016, 2016.

Nowlan, C., González Abad, G., Kwon, H., Ayazpour, A., Chan Miller, C., Chance, K., Chong, H., Liu, X., O'Sullivan, E., Wang, H., Zhu, L., De Smedt, I., Jaross, G., Seftor, C., Sun, K.: Global formaldehyde products from the Ozone Mapping and Profiler Suite (OMPS) nadir mappers on Suomi NPP and NOAA-20, Earth and Space Science, 19, https://doi.org/10.1002/essoar.10512639.1, 2022.

Palmer, P. I., Jacob, D. J., Chance, K., Martin, R. V., Spurr, R. J., Kurosu, T. P., et al.: Air mass factor formulation for spectroscopic measurements from satellites: Application to formaldehyde retrievals from the Global Ozone Monitoring Experiment. J. Geophys. Res. – Atmos., 106 (D13), 14539-14550, https://doi.org/10.1029/2000JD900772, 2001.

Qin, W., Fasnacht, Z., Haffner, D., Vasilkov, A., Joiner, J., Krotkov, N., Fisher, B., and Spurr, R.: A geometry-dependent surface Lambertian-equivalent reflectivity product for UV-Vis retrievals – Part 1: Evaluation over land surfaces using measurements from OMI at 466 nm., Atmos. Meas. Tech., 12, 3997-4017, https://doi.org/10.5194/amt-12-3997-2019, 2019.

Richter, A., Begoin, M., Hilboll, A., Burrows, J. P.: An improved NO2 retrieval for the GOME-2 satellite instrument, Atmos. Meas. Tech., 4, 1147-1159, https://doi.org10.5194/amt-4-1147-2011.

https://doi.org/10.5194/amt-2023-66
Preprint. Discussion started: 27 June 2023

Atmospheric Measurement Techniques Discussions

Schaaf, C., and Wang, Z.: MCD43C1 MODIS/Terra+Aqua BRDF/Albedo Model Parameters Daily L3 Global 0.05Deg CMG V006 [dataset]. NASA EOSDIS Land Processes DAAC, https://doi.org/10.5067/MODIS/MCD43C1.006, 2015.

Schröder, M., Lockhoff, M., Fell, F., Forsythe, J., Trent, T., Bennartz, R., Borbas, E., Bosilvich, M. G., Castelli, E., Hersbach, H., Kachi, M., Kobayashi, S., Kursinski, E. R., Loyola, D., Mears, C., Preusker,, R., Rossow, W. B., and Saha, S: The GEWEX water vapor assessment archive of water vapour products from satellite observations and reanalyses. Earth Syst. Sci. Data, 10, 1093-1117, https://doi.org/5194/essd-10-1093-2018, 2018.

Serdyuchenko, A., Gorshelev, V., Weber, M., Chehade, W., & Burrows, J. P.: High spectral resolution ozone absorption cross-sections – Part 2: Temperature dependence, Atmos. Meas. Tech., 7 (2), 625-626, doi:10.5194/amt-7-625-2014, 2014.

Spietz, P., Martian, J. C. G., and Burrows, J. P., 2005. Spectroscopic studies of the I-2/O-3 photochemistry – Part 2. Improved spectra of iodine oxides and analysis of the IO absorption spectrum, J. Photochemistry and Photobiology A – Chemistry, 176, 1-3, 50-67, https://doi.org/10.1016/j.jphotochem.2005.08.023, 2005.

Spurr, R.: VLIDORT: A linearized pseudo-spherical vector discrete ordinate radiative transfer code for forward model and retrieval studies in multilayer multiple scattering media. Journal of Quantitative Spectroscopy and Radiative Transfer, 102 (2), 316-342, https://Doi.org/10.1016/j.jqsrt.2006.05.005, 2006.

Spurr, R.: LIDORT and VLIDORT: Linearized pseudo-spherical scalar and vector discrete ordinate radiative transfer models for use in remote sensing retrieval problems. In Light Scattering Reviews 3: Light Scattering and Re-flection (pp. 229-275, Berlin, Heidelberg: Springer Berlin Heidelberg, https://doi.org/10.1007/978-3-540-48546-9_7, 2008.

Spurr, R, and M. Christi: The LIDORT and VLIDORT Linearized Scalar and Vector Discrete Ordinate Radiative Transfer Models: Updates in the last 10 Years. Light Scattering Reviews, Volume 12, ed. A. Kokhanovsky, Springer, 2019.

Sun, K., Liu, X., Huang, G., González Abad, G., Cai, Z., Chance, K., and Yang, K.: Deriving the slit functions from OMI solar observations and its implications for ozone-profile retrieval, Atmos. Meas. Tech., 10, 3677-3695, https://doi.org/10.5194/amt-10-3677-2017, 2017.

Thompson, D. R., Kahn, B. H., Brodrick, P. G., Lebsock, M. D., Richardson, M., and Green, R. O.: Spectroscopic imaging of sub-kilometer spatial structure in lower-tropospheric water vapor, Atmos. Meas. Tech., 14, 2827-2840, https://doi.org/10.5194/amt-14-2827-2021, 2021.

Vandaele, A. C., Hermas, C., Simon, P. C., Carleer, M., Colin, R., Fally, S., Merienne, M. F., Jenouvier, A. and Coquart, B.: Measurements of the NO2 absorption cross-section from 42000 cm(-1) to 10000 cm(-1) (238-1000 nm) at 200 K and 294 K, J. Quant. Spectr. Radiat. Trans., 59, 171-184, https://doi.org/10.1016/S0022-4073(97)00168-4, 1998.

Vasilkov, A., Krotkov, N., Yang, E., Lamsal, L., Joiner, J., Castellanos, P., Fasnacht, Z., and Spurr, R.: Explicit and consistent aerosol correction for visible wavelength satellite cloud and nitrogen dioxide retrievals based on optical properties from a global aerosol analysis, Atmos. Meas. Tech., 14, 2857-2871, https://doi.org/10.5194/amt-14-2857-2021, 2021.

Veefkind, J. P., de Hann, J. F., Sneep, M. and Levelt, P. F.: Improvements to the OMI O2-O2 operational cloud algorithm and comparisons with ground-based radar-lidar observations, Atmos. Meas. Tech., 9, 6035-6049, https://doi.org/10.5194/amt-9-6035-2016, 2016.

Volkamer, R., Spietz, P., Burrows, J. and Platt, U.: High-resolution absorption cross section of glyoxal in the UV/Vis and IR spectral ranges, J. Photochem. Photobio., 172, 35-46, https://doi.org/10.1016/j.jphotochem.2004.11.011, 2005.

Wagner, T., Beirle, S., Sihler, H. and Mies, K.: A feasibility study for the retrieval of the total column precipitable water vapour from satellite observations in the blue spectral range, Atmos. Meas. Tech., 6, 2593-2605, https://doi.org/10.5194/amt-6-2593-2013, 2013.

Wang, H., Liu, X., Chance, K., González Abad, G., Chan Miller, C.: Water vapor retrieval from OMI visible spectra, Atmos. Meas. Tech., 7 (6), 1901-1913, https://doi.org/10.5194/amt-7-1901-2014, 2014.

Wang, H., González Abad, G., Liu, X., Chance, K.: Validation and update of OMI total column water vapor product, Atmos. Chem. Phys. 16 (17), 11379-11393, https://doi.org/10.5194/acp-16-11379-2016, 2016.

https://doi.org/10.5194/amt-2023-66
Preprint. Discussion started: 27 June 2023

Wang, H., Souri, A. H., González Abad, G., Liu, X., Chance, K.: Ozone Monitoring Instrument (OMI) total column water vapor version 4 validation and applications. Atmos. Meas. Tech., 12 (9), 5183-5199, https://doi.org/10.5194/amt-12-5183-2019, 2019.

Wang, H., González Abad, G., Chan Miller, C., Kwon, H., Nowlan, C. R., Ayazpour, Z., Chong, H., Liu, X., Chance, K., O'Sullivan, E., Sun, K., Spurr, R., Hargreaves, R. J.: MEaSUREs blue band total column water vapor sample data for the Ozone Monitoring Instrument. Zenodo, https://doi.org/10.5281/zenodo.7795648, 2023.

Wang, J., Zhang, L., Dai, A., Van Hove, T., Van Baelen, J.: A near-global, 2-hourly data set of atmospheric precipitable water from ground-based GPS measurements. J. Geophys. Res. – Atmos., 112, D11, D11107, https://doi.org/10.1029/2006JD007529, 2007.

Wang, Z., Schaaf, C. B., Sun, Q., Shuai, Y., and Román, M. O.: Capturing rapid land surface dynamics with Collection V006 MODIS BRDF/NBAR/Albedo (MCD43) products, Remote Sensing of Environment, 207, 50-64, https://doi.org/10.1016/j.rse.2018.02.001, 2018.

Wentz, F. J., C. L. Gentemann and K. A. Hilburn: Three years of ocean products from AMSR-E: Evaluation and applications, Proceedings of the 2005 IEEE International Geoscience and Remote Sensing Symposium, Seoul, Korea, 2005.

Wentz, F.J., T. Meissner, C. Gentemann, M.Brewer: Remote Sensing Systems AQUA AMSR-E Daily Environmental Suite on 0.25 deg grid, Version 7. Remote Sensing Systems, Santa Rosa, CA. Available online at www.remss.com/missions/amsr, 2014

Zoogman, P., Liu, X., Chance, K., Sun, Q., Schaaf, C., Mahr, T., and Wagner, T.: A climatology of visible surface reflectance spectra, Journal of Quantitative Spectroscopy and Radiative Transfer, 180, 39-46, https://doi.org/1266 10.1016/j.jqsrt.2016.04.003, 2016.